

A Very Impressive and Fancy Title for a Thesis

by

Giovanni Pederiva

THESIS
for the degree of
MASTER OF SCIENCE



Faculty of Mathematics and Natural Sciences
University of Oslo

May 2018

Contents

I Introduction to QCD and Lattice Field Theories	5
1 A Primer on QCD in the Continuum	7
1.1 The QCD Lagrangian	8
1.1.1 Feynman Rules of QCD	9
1.1.2 Gauge Symmetry of the Lagrangian	11
1.2 General Properties of QCD	12
1.2.1 Running Coupling	12
1.3 Methods and Regimes of Chromodynamics	15
2 Lattice Field Theories and Lattice QCD	19
2.1 Discretizing Field Theories	19
2.1.1 The Harmonic Oscillator Example	20
2.2 Discretization of QCD on the Lattice	20
2.2.1 Naïve Discretization of Fermions	20
2.2.2 The Gauge Transporter and the Wilson Loop	21
2.2.3 Lattice Fermions	23
2.3 Path Integrals on the Lattice	24
2.3.1 Pure Gauge Field Theory	25
2.3.2 Observables	25

2.4	Modern Lattice QCD Calculations	28
3	Advanced Topics in Lattice QCD	31
3.1	Scale Setting in the Quenched Approximation	31
3.2	The Gradient Flow Method	32
3.3	Perturbative Analysis of the Wilson Flow	33
3.3.1	Scale Fixing with the Gradient Flow	34
3.4	Estimating the Scale Parameter	36
3.4.1	4-loop Corrected Running Coupling	36
II	Implementation	39
4	Designing a Lattice $SU(3)$ Yang-Mills Theory Code	41
4.1	Generating Pure Gauge Fields	41
4.1.1	The Metropolis Algorithm	42
4.1.2	Sampling the Configuration Space	44
4.1.3	Updates Strategies	45
4.1.4	Parallelization Scheme	46
4.1.5	Summary of the Parameters	47
4.2	Wilson Flow of Gauge Configurations	47
4.2.1	The Action Derivative	48
4.2.2	Exponential of a $\mathfrak{su}(3)$ Element	48
4.2.3	Parallelization Scheme	49
4.3	Structure and Tools	51
5	Tests and Runs Description	53
5.1	Generated Ensembles	53

5.2	Test Runs	54
5.2.1	Thermalization	55
5.2.2	Tests on the Autocorrelation of Observables	56
5.2.3	Strong and Weak Scaling	58
5.3	Production Runs and Timing	58
 III Data Analysis and Results		 61
 6	Raw Observables	 63
6.1	Plaquette and Energy Density	63
6.2	Topological Charge	64
6.3	Topological Susceptiblity	70
 7	Running Coupling and Scale Fixing	 73
7.1	Discretization Effects on $t_f^2 \langle E \rangle$	73
7.2	Matching Perturbative and Lattice Results	75
7.2.1	Strategy for the Estimation of the Scale Energy Λ	75
 IV Conclusions		 77
 8	Summary and Outlook	 79
 V	Appendices	 81
 Appendix A	Statistical Tools	 83

Abstract

some abstract

Acknowledgements

Part I

Introduction to QCD and Lattice Field Theories

Chapter 1

A Primer on QCD in the Continuum

The Standard Model of particle physics (SM) is the theory of fundamental particles and their interactions. Three of the four known fundamental forces are described by it, the exception is Gravity, so that all phenomena regarding the Electromagnetic, Weak and Strong forces are included within the theory.

The SM describes quantized fields defined on all space-time whose excitations are commonly identified with particles. There are two categories of fields, depending on the spin statistic they can be: fermions, quarks or leptons in the SM, which are the constituents of matter; or bosons, which mediate the interactions between particles.

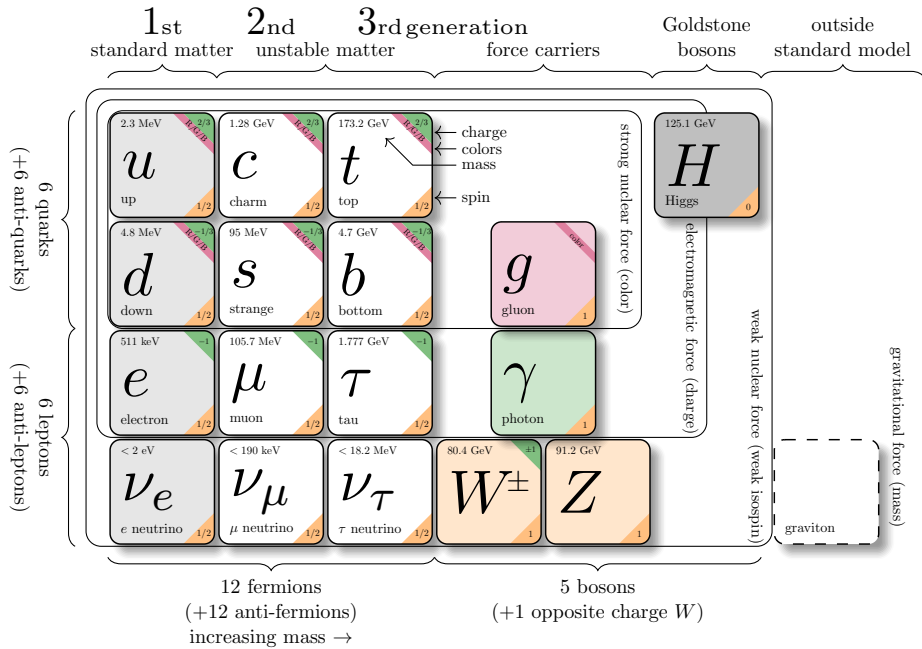


Figure 1.1: Summary of the particles on the Standard Model [1]

From a group theory point of view, the SM is the composition of three different local gauge symmetry groups, each associated with a fundamental force:

$$SU(3)_C \times \underbrace{SU(2)_L \times U(1)_Y}_{\text{broken to } SU(2)_W \times U(1)_Q} \quad (1.1)$$

The $U(1)_Q$ symmetry group is associated with the electromagnetic interaction and $SU(2)_W$ is the weak interaction. They both derive from the symmetry $SU(2)_L \times U(1)_Y$, which is spontaneously broken through the Higgs Mechanism, that defines the unified electroweak theory. Quantum Chromodynamics, commonly referred to as QCD, is the quantum field theory, contained in the SM, that describes the behavior of strongly interacting matter, that is quarks and gluons. It is a non-abelian gauge theory based on a $SU(3)$ symmetry group. The associated quantum number is called “color charge” which pictorially can assume the values of *red* (r), *green* (g), *blue* (b), *anti-red* (\bar{r}), *anti-green* (\bar{g}) or *anti-blue* (\bar{b}). In this chapter, we will discuss the QCD Lagrangian density, its properties and some of the major results of the theory. Some intermediate knowledge of Quantum Field Theory is assumed and derivations and proofs mainly follow the reasoning found in [2].

1.1 The QCD Lagrangian

In Quantum Field Theory (QFT) the characterizing equation of a theory is its Lagrangian density because it contains all the information about the fields that are involved, their properties and most importantly, their interactions. QCD is a non-abelian gauge theory based on the $SU(3)$ local gauge symmetry group. The simplest Lagrangian is the Yang-Mills Lagrangian:

$$\mathcal{L}_{QCD} = + \sum_{f=1}^{N_f} \bar{\psi}_f (i\gamma^\mu D_\mu - m_f) \psi_f - \frac{1}{4} (G_{\mu\nu}^a)^2 \quad (1.2)$$

Here ψ_f and $\bar{\psi}$ represent the complex-valued fermion fields of flavor f , with mass m_f . These are associated with the quark fields and come in six flavors: *u* (up), *d* (down), *s* (strange), *c* (charm), *b* (bottom) and *t* (top). The second element in the Lagrangian is the Gluon Field Strength Tensor, $G_{\mu\nu}^a$. The two indices μ and ν are Lorentz and γ^μ are Dirac’s matrices. a is the index of the generators of the gauge group, $SU(3)$ in this case. Note that Einstein’s summing convention on repeated indices is implicit, for example when taking the square of the field strength tensor three sums are applied. The definition of $G_{\mu\nu}^a$ is:

$$G_{\mu\nu}^a = \frac{i}{g_0} [D_\mu, D_\nu] = \partial_\mu A_\nu^a - \partial_\nu A_\mu^a + g_0 f^{abc} A_\mu^b A_\nu^c \quad (1.3)$$

In this equation A_μ^a is the gluon field, that carries a Lorentz index and a group generator index, g_0 is the bare coupling constant of the strong interaction and the f^{abc} are the structure constants of $SU(3)$, which satisfy:

$$[t^a, t^b] = i f^{abc} t^c \quad (1.4)$$

with t^a being the generators of the algebra $\mathfrak{su}(3)$. The covariant derivative D_μ is defined to be:

$$D_\mu = \partial_\mu - ig_0 t^a A_\mu^a \quad (1.5)$$

With the information contained in the Lagrangian density, the behavior and the interactions of all fields are set.

1.1.1 Feynman Rules of QCD

A key element that is needed to perform perturbative calculations in a quantum field theory are Feynman Rules. These are a set of equations and rules that represent the propagation of fields and the interaction vertices of the theory. For the case of QCD, being a non-abelian gauge theory, some vertices represent interactions between gauge bosons only, as opposed to Quantum Electrodynamics, QED, that forbids photon-photon interactions.

To begin with, we need to write out all of the terms of the Lagrangian density individually. We assume only one quark flavor as no term in the Lagrangian can change this quantum number.

$$\begin{aligned} \mathcal{L}_{QCD} &= \bar{\psi}(i\gamma^\mu D_\mu - m)\psi - \frac{1}{4}(G_{\mu\nu}^a)^2 \\ &= \bar{\psi}(i\gamma^\mu \partial_\mu + g_0 \gamma^\mu t^a A_\mu^a - m)\psi \\ &\quad - \frac{1}{4}(\partial_\mu A_\nu^a - \partial_\nu A_\mu^a + g_0 f^{abc} A_\mu^b A_\nu^c)(\partial_\mu A_\nu^a - \partial_\nu A_\mu^a + g_0 f^{ade} A_\mu^d A_\nu^e) \\ &= \bar{\psi}(i\gamma^\mu \partial_\mu - m)\psi \\ &\quad - \frac{1}{4}(\partial_\mu A_\nu^a - \partial_\nu A_\mu^a)^2 \\ &\quad - g_0 f^{abc} (\partial_\mu A_\nu^a) A^{b\mu} A^{c\nu} \\ &\quad - \frac{1}{4} g_0^2 f^{abc} f^{ade} A_\mu^b A_\nu^c A^{d\mu} A^{e\nu} \\ &\quad + g_0 \gamma^\mu t^a A_\mu^a \bar{\psi}\psi \end{aligned} \quad (1.6)$$

The first thing to do is to define the quark and gluon propagators, which can be obtained from the first and second terms respectively of the last equality:

$$\begin{aligned} i \xrightarrow[k]{\longrightarrow} j &= \frac{i(\gamma^\mu k_\mu + m)}{k^2 - m + i\epsilon} \delta_{ij} \\ a_\mu \xrightarrow[k]{\swarrow\searrow} b_\nu &= -\frac{i}{k^2 + i\epsilon} \delta_{ab} g^{\mu\nu} \end{aligned}$$

with $g^{\mu\nu}$ being the metric tensor of Minkovskian space-time. The third term in eq. (1.6) represents a three gluon vertex:

$$= g_0 f^{abc} [g^{\mu\nu}(p-q)^\rho + g^{\nu\rho}(q-k)^\mu + g^{\rho\mu}(k-p)^\nu]$$

Then the four-gluon vertex:

$$= -ig_0^2 [f^{abe} f^{acd} (g^{\mu\nu} g^{\sigma\rho} - g^{\mu\rho} g^{\nu\sigma}) + f^{abd} f^{ace} (g^{\mu\nu} g^{\sigma\rho} - g^{\mu\sigma} g^{\nu\rho}) + f^{abc} f^{aed} (g^{\mu\sigma} g^{\nu\rho} - g^{\mu\rho} g^{\nu\sigma})]$$

Finally we have the gluon-quark interaction vertex:

$$= ig_0 t^a \gamma^\mu$$

Note that the Lagrangian we considered, and the resulting Feynman rules, is over-simplified: the “full” Lagrangian contains terms from Faddeev-Popov ghosts, that are introduced to fix the problems that arise when fixing the gauge; and counter-terms from the renormalization procedure. Nevertheless, interesting qualitative features can be inferred from the Feynman rules: the fact that gluons interact with each other through the three- and four-gluon vertices; the non flavor-changing interaction between gluons and quarks, which decouples completely different quark flavors; the “color-changing nature” of the quark-gluon interaction, given by the t^a matrix in the vertex term that shows how the color state of a fermion is changed by the absorption or emission of a gluon.

1.1.2 Gauge Symmetry of the Lagrangian

The concept of gauge invariance is crucial in the construction of a discretized lattice theory from the continuum one, so it is worth considering how it is introduced. The QCD Lagrangian must be gauge invariant to be physical, not only on a global scale, but it must be locally invariant. Let's consider a quark field $\psi(x)$, which truly is a triplet of fermion fields each with different color quantum number:

$$\psi(x) = \begin{pmatrix} \psi_r(x) \\ \psi_b(x) \\ \psi_g(x) \end{pmatrix} \quad (1.7)$$

A local gauge transformation in the internal space of $SU(3)$ is a unitary transformation of this 3-component vector, a rotation in color space. Defining $\Omega(x)$ one such local transformation applied to $\psi(x)$ one has:

$$\psi(x) \rightarrow \psi'(x) = \Omega(x)\psi(x) \quad (1.8)$$

and for the Dirac adjoint:

$$\bar{\psi}(x) \rightarrow \bar{\psi}'(x) = \bar{\psi}(x)\Omega^\dagger(x) \quad (1.9)$$

The transformation can be parametrized in terms of some functions $\alpha^a(x)$, one for each generator of the group:

$$\Omega(x) = \exp[i\alpha^a(x)t^a] \quad (1.10)$$

This internal space rotation if applied to the simple Dirac free-field Lagrangian would generate an additional term:

$$\begin{aligned} \mathcal{L}_{Dirac} &= \bar{\psi}(i\gamma^\mu \partial_\mu - m)\psi \rightarrow \mathcal{L}'_{Dirac} = \bar{\psi}\Omega^\dagger(i\gamma^\mu \partial_\mu - m)(\Omega\psi) \\ &= \bar{\psi}'(i\gamma^\mu \partial_\mu - m)\psi' + i\bar{\psi}'\gamma^\mu\psi(\partial_\mu\Omega) \end{aligned} \quad (1.11)$$

The extra term implies that Dirac lagrangian is not gauge invariant. In order to fix this problem a new field $A_\mu(x)$, the gauge field, and it is convention to include it into the definition of the covariant derivative, so that ∂_μ becomes $D_\mu = \partial_\mu - ig_0 A_\mu(x)$, as previously stated; D_μ represents the derivative along the tangent vectors of the manifold on which the field is defined. The field $A_\mu(x)$ is algebra-valued and, to be consistent with the previous section one need to project it on a basis of generators of the group: $A_\mu(x) = A_\mu^a(x)t^a$ (remember the implicit sum).

The transformation rule for $A_\mu(x)$ is fixed in order to cancel the extra term in eq. (1.11) exactly, such that:

$$D_\mu\psi \rightarrow (D_\mu\psi)' = (\partial_\mu - ig_0 A'_\mu(x))\psi' = \Omega(D_\mu\psi) \quad (1.12)$$

and this fixes the transformation for $A_\mu(x)$ to be:

$$A_\mu(x) \rightarrow A'_\mu(x) = \Omega \left[A_\mu(x) + \frac{i}{g_0} \Omega^\dagger \partial_\mu \Omega \right] \Omega^\dagger \quad (1.13)$$

we can see that the last term contributes effectively to the Lagrangian as $-i\bar{\psi}'\gamma^\mu\psi(\partial_\mu\Omega)$, which is what we wanted to cancel. For an infinitesimal transformation we can expand the matrix Ω in powers of α as $\Omega(x) = \exp[i\alpha^a(x)t^a] \approx 1 + i\alpha^a(x)t^a$ and get the following for the gauge field transformation, for a single component:

$$A_\mu^a(x) \rightarrow A'^a_\mu(x) = A_\mu^a(x) + \frac{i}{g_0} \partial_\mu \alpha^a(x) + f^{abc} A_\mu^b(x) \alpha^c(x) \quad (1.14)$$

which is the last element needed. One can now look at all the possible gauge invariant objects that can be constructed with the fields ψ and A of dimension 4, the same of the Lagrangian. Apart from the one already present in the Dirac Lagrangian with the covariant derivative, there are only two additional terms that are gauge invariant and of dimension 4 and they both can be taken by considering the gauge field tensor:

$$G_{\mu\nu}^a \equiv \frac{i}{g_0} [D_\mu, D_\nu] = \partial_\mu A_\nu^a - \partial_\nu A_\mu^a + g_0 f^{abc} A_\mu^b A_\nu^c \quad (1.15)$$

this is clearly gauge invariant since it is the commutator of covariant derivatives and it has dimension 2. One can now construct the gauge field kinetic term, the well known $-\frac{1}{4}(G_{\mu\nu}^a)^2$ and reconstruct eq. (1.2). However, there is an additional term, not included in the QCD Lagrangian, that is the “dual term”, or “theta term” which will be interesting further in the work. It is defined as $\theta G_{\mu\nu}^a \tilde{G}^{a\mu\nu}$ where $\tilde{G}^{a\mu\nu} = \epsilon^{\mu\nu\rho\sigma} G_{a\rho\sigma}$ is the dual of the field tensor and $\epsilon_{\mu\nu\rho\sigma}$ the anti-symmetric Levi-Civita tensor of rank 4. With it the Lagrangian becomes:

$$\mathcal{L}_{QCD} = -\frac{1}{4}(G_{\mu\nu}^a)^2 + \bar{\psi}(i\cancel{D} - m)\psi + \theta G_{\mu\nu}^a \tilde{G}^{a\mu\nu} \quad (1.16)$$

The theta term is usually neglected because there is no experimental evidence of it, but in principle it cannot be excluded. It is the simplest CP violating term that can be added to the QCD Lagrangian and for this is of particular interest in the study of CP phenomena, like the nucleon electric dipole moment (EDM)[3].

1.2 General Properties of QCD

Quantum Chromodynamics exhibits a set of features as a theory that is common to all non-abelian gauge theories. We have already seen one, that is the direct interaction of the gauge bosons, something that is not allowed in abelian theories as QED. Other interesting properties emerge when trying to renormalize the theory and are in general linked to the fixing of the scale, which leads to the concept of running coupling. In the particular case of QCD, the coupling constant at in a low-energy regime leads to Confinement, while in the high-energy limit Asymptotic Freedom emerges.

1.2.1 Running Coupling

The Renormalization Group Equation (RGE) defines the rate at which the renormalized coupling g varies as the renormalization scale of μ changes, through the beta function of the coupling constant, $\beta(g)$.

$$\beta(g) = \frac{d}{d\log(\mu)} g(\mu) \quad (1.17)$$

For a generic non-abelian theory $SU(N)$ one can expand the β function in orders of g as:

$$\beta(g) = b_0 g^3 + b_1 g^5 + b_2 g^7 + \dots \quad (1.18)$$

One can then integrate up to arbitrary order eq. (1.17) and get an expression for $g(\mu)$. The coefficients b_i are obtained from computing contribution of higher and higher diagrams to the coupling. The value of b_0 , from 1-loop corrections, is:

$$b_0 = -\frac{1}{(4\pi)^2} \left(\frac{11}{3}N - \frac{2}{3}N_f \right) \quad (1.19)$$

Here N is the gauge group $SU(N)$ dimension and N_f the number of flavors of the fermions. The minus sign in front implies that any non-abelian theory with a sufficiently small number of fermions, less than $\frac{11}{2}N$ (that is 16 for QCD), is “asymptotically free”, meaning that at high energy the coupling vanishes and particles don’t feel any interaction.

The RGE is usually expressed in terms of the analog of the fine structure-constant for the strong force, $\alpha_s = g^2/4\pi$. The first order solution is given by plugging eq. (1.19) into eq. (1.17) and integrating. In terms of α_s at a scale μ we get:

$$\alpha_s(\mu) = \frac{\alpha_s^0}{1 + \frac{b_0\alpha_s^0}{4\pi} \log(\mu^2/M^2)} \quad (1.20)$$

here α_s^0 is the value of the coupling at an energy M , which is set by the integration. The typical choice for M when measuring experimentally the running coupling is the mass of the Z boson, where QCD can be compared relatively simply to the other forces and experimental precision is high. The coupling depends on an arbitrarily chosen renormalization point M , so a convenient choice is rewrite the equation in simpler way defining a momentum scale Λ that satisfies:

$$1 = \frac{b_0\alpha_s^0}{4\pi} \log(M^2/\Lambda^2) \quad (1.21)$$

This simplifies eq. (1.20) to its well-known form, correct up to one loop corrections:

$$\alpha_s(\mu) = \frac{4\pi}{b_0 \log(\mu^2/\Lambda^2)} \quad (1.22)$$

In fig. 1.2 a higher order approximation of $\alpha_s(\mu)$ is plotted against some experimental values. In section 3.4.1 we will show a more precise result, correct up to 4 loop corrections, of this result. The momentum scale, often referred to as Λ_{QCD} , is the energy at which the interactions become strong. Experimental values [5] suggest that $\Lambda_{QCD} \approx 200 - 300$ MeV, meaning that perturbation theory can be safely applied from momenta roughly above the 1 GeV scale, where $\alpha_s \approx 0.4$.

One of the main goals for this thesis is to find a simple and not expensive way to estimate the mass scale parameter Λ from lattice calculations, in this work on pure Yang-Mills theory, that means with no fermion flavors, and in prospect for QCD with 2 or 2 + 1 dynamical fermions.

Asymptotic Freedom

Equation (1.22) is a clear indication that QCD at high energies has a small coupling. Asymptotic freedom is the property of gauge theories, QCD is usually the example of it, that causes the interactions between the fields do become weaker as the energy scale increases and this is because

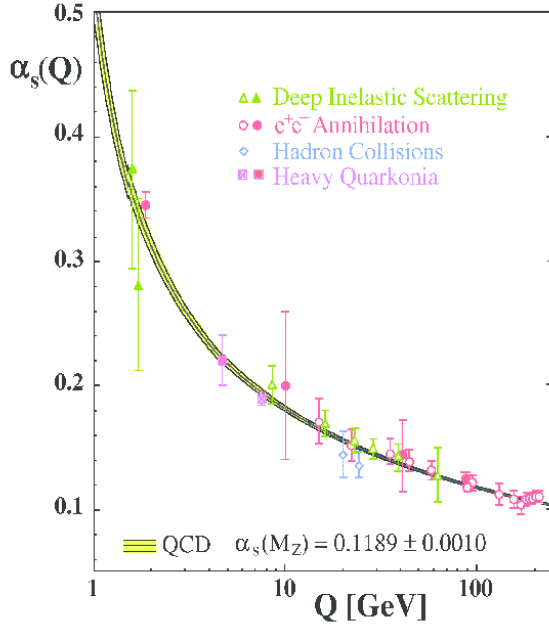


Figure 1.2: The strong coupling as a function of the energy scale. The data points are experimental results; the black solid line and yellow bands represent the QCD prediction using the reported value of the coupling at the mass of the Z boson (α_s^0 in our notation). Image from [4]

of the inverse log dependence of the coupling on the energy. This is, for example, one of the bases on which Grand Unification Theories (GUT) are based on, the fact that there exists an energy scale at which the strong force has a coupling equivalent to the one of the electroweak interaction.

The discovery of asymptotic freedom by Gross, Wilczek and Politzer [6][7], was used as an indication that QCD is indeed the correct theory of the strong interaction in the late Seventies, when the fundamental theory was still debated.

Asymptotically free theories can be analyzed perturbatively at sufficiently large energies and are believed to be consistent up to any energy scale.

Confinement

In general, color charged particles cannot be isolated, so that quarks and gluons are not detectable alone, but always in the form of hadrons: colorless objects formed of multiple quarks, mesons (quark-antiquark) and hadrons (three quarks or three anti-quarks). Glueballs, combinations of gluons such that the total is colorless, are also in principle allowed, but have not been observed yet. Confinement is the phenomenon for which it is not possible to isolate a color charge, single quarks or gluons, from a hadron without producing other new hadrons. Single colored particles in a very small time scale undergo hadronization, the process of spawning new quarks or anti-quarks from the vacuum to balance the total color charge and produce colorless matter. This is the reason for the fundamentally different nature of the strong force compared

to the other forces, no perturbative expansion can be made at low energies. The exact proof of how this links with the color confinement of QCD is yet not known, but qualitatively it can be explained by the fact that the gauge bosons of the theory, the gluons, carry color charge just like the quarks.

At low energy scales from eq. (1.22) we can infer that the coupling constant increases exponentially, so particles that have energies comparable to the energy scale Λ_{QCD} interact very strongly with the gauge field and any other particle. This implies, for example, that the force between two particles does not vanish for long distances, but instead it increases. The usual picture is to consider the gluons being exchanged by two quarks at rest. These gluons would form flux-tubes between the sources that, if stretched by separating the quarks, eventually store enough energy to make a quark-anti-quark pair energetically favorable.



Figure 1.3: Representation of confinement using flux-tubes . As two color sources are pulled apart, the energy stored in the color field between the sources increases so much that a $q\bar{q}$ pair is formed from the vacuum energy.

One could also look at the inverse of the energy scale, which is a distance in natural units, of roughly $\Lambda_{QCD}^{-1} \approx 1fm$, that is approximately the size of light hadrons, a further proof that quark sources cannot be torn apart easily.

The strong low-energy interaction is the cause for the large discrepancy between the mass of the baryons and the mass of their constituent quarks. For the proton for example, the quark masses (2 up-quarks and 1 down-quark) give a total of 10 MeV, while the mass of the proton is 938 MeV. This means that the 99% of the mass of the proton is given by the quark and gluon binding energy.

1.3 Methods and Regimes of Chromodynamics

Given the very different behaviors of the strong force at different energy scales, QCD needs to be dealt with in various ways depending on the scale of interest. At high energies, perturbation theory can be applied safely, but at low ones no expansion in the coupling constant can be made.

Perturbative QCD

At high energies, like the scale of the large particle accelerators that are currently available, the QCD coupling constant is sufficiently small to allow analytical calculations of Feynman diagrams to be meaningful. Hadronization is neglected as the time scale is small enough to consider it

a post-collision process. For example, at a scale where the strong force is comparable to the electroweak interaction, the cross section of $e^+e^- \rightarrow \text{hadrons}$ compared to that of $e^+e^- \rightarrow \mu^+\mu^-$ can be used to measure the number of quark flavors that are active below that energy. Figure (1.4) the perturbative QCD cross section for the process is shown compared to experimental data.

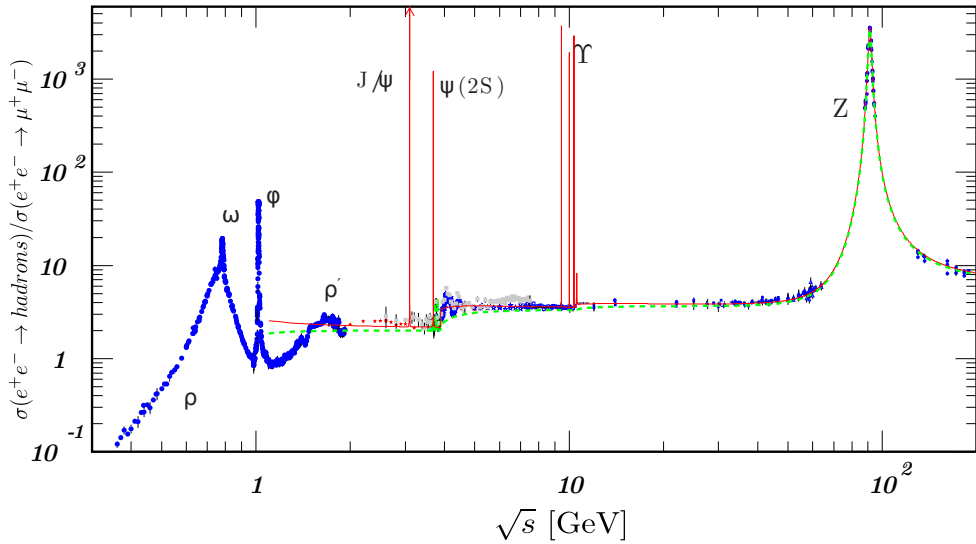


Figure 1.4: Ratio of the experimental cross section of $e^+e^- \rightarrow \text{hadrons}$ and $e^+e^- \rightarrow \mu^+\mu^-$ as collected by the Particle Data Group. Naive quark model is the dashed green line and pQCD results are also shown as a solid red line. pQCD appear to agree well to experiment in non resonant regions of the energy spectrum. The steps are given by the energy threshold of different quark flavors.

Lattice Methods

To deal with the non-perturbative sector of the strong interaction the most widespread approach is to use numerical simulations, in particular, lattice methods, so it is common to refer to it as Lattice QCD. The main idea, which will be expressed more in detail in Chapter 2, is to discretize space-time and evaluate the field only at fixed sites on a hyper-cubic lattice, physical quantities are then computed stochastically on ensembles of such gauge fields. This approach, however, is very expensive from a computational point of view and so far no calculation at physical quark masses with a sufficiently small lattice spacing, in principle closer to the continuum theory, have been performed.

Effective Field Theories

An interesting problem is to link QCD directly with nuclear forces, that are long-range remnants of the strong interaction at a hadron level. The problem is of high interest because there is yet no fundamental theory of nuclear interactions from first principles. The most common

approach is to define an Effective Field Theory, starting from a low energy approximation of chromodynamics, that preserves most of the symmetries of the underlying theory.

Chiral EFT (χ EFT) is one of the most popular of such theories; it starts from considering nucleons as a fundamental $SU(2)$ group in isospin and describes the interactions between them through the exchange of pions [8]. It promotes particles that are not fundamental in QCD to the basic blocks of a low-energy effective Lagrangian, with nucleons as the fermion fields and pions as Nambu-Goldstone bosons of the theory. Its Lagrangian is constructed in a systematic manner considering all possible interaction vertices between hadrons:

$$\mathcal{L}_{\chi EFT} = \mathcal{L}_{\pi\pi} + \mathcal{L}_{\pi N} + \mathcal{L}_{NN} + (\text{three hadron terms}) + \dots \quad (1.23)$$

where $\mathcal{L}_{\pi\pi}$ is the term describing the dynamics between pion, \mathcal{L}_{NN} the term for interactions between two nucleons, $\mathcal{L}_{\pi N}$ the one between one pion and one nucleon and so on. Each term is further expanded in powers of Q/Λ_χ where Q is the pion momentum and Λ_χ is the energy scale at which the theory breaks down because of the pions acquiring an energy comparable to the mass of the nucleons. One constructs order by order all possible terms:

$$\begin{aligned} \mathcal{L}_{NN} &= \mathcal{L}_{NN}^{(0)} + \mathcal{L}_{NN}^{(2)} + \mathcal{L}_{NN}^{(4)} + \dots \\ \mathcal{L}_{\pi N} &= \mathcal{L}_{\pi N}^{(1)} + \mathcal{L}_{\pi N}^{(2)} + \mathcal{L}_{\pi N}^{(3)} + \mathcal{L}_{\pi N}^{(4)} + \dots \\ \mathcal{L}_{\pi\pi} &= \mathcal{L}_{\pi\pi}^{(2)} + \mathcal{L}_{\pi\pi}^{(4)} + \dots \end{aligned} \quad (1.24)$$

one then computes all possible diagrams order by order and truncates the expansion when needed. This is mostly useful for computing reduced matrix elements for many-body nuclear calculations.

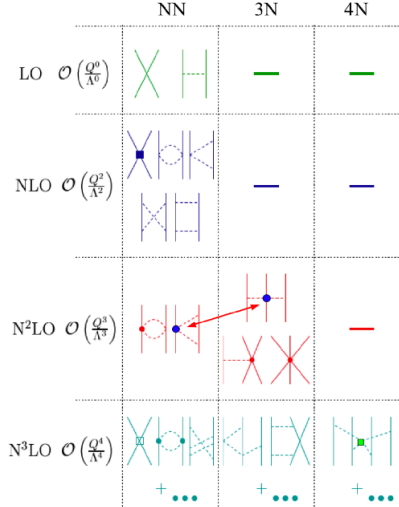


Figure 1.5: Diagrams of the leading order terms in χ EFT. [9]

One interesting remark, as seen in fig. 1.5 is that the approach of χ EFT spontaneously generates interaction matrix elements for three or more nucleons.

Chapter 2

Lattice Field Theories and Lattice QCD

Lattice QCD is one of the main Lattice Field Theories. It deals with the strong force in a numerical way. The idea of discretizing space-time in a lattice and perform calculations of field theories was proposed by Wilson in 1974 [10] as an alternative method to explain confinement. It has proven to be the most systematic approach to non-perturbative theories like QCD. In this chapter we will describe briefly how this discretization procedure is performed and some of the main computational strategies that are involved.

2.1 Discretizing Field Theories

The starting point for Lattice QCD is Feynman's path-integral formalism, but expressed in Euclidean space-time, through a Wick rotation. An observable of some field ϕ is then given by:

$$\langle O[\phi] \rangle = \frac{1}{Z[\phi]} \int \mathcal{D}[\phi] O[\phi] e^{-S[\phi]} \quad (2.1)$$

where the partition function $Z[\phi]$ is defined as:

$$Z = \int \mathcal{D}[\phi] e^{-S[\phi]} \quad (2.2)$$

and $S[\phi]$ is the classical action of the field. Evaluating path-integrals is not possible in general with analytical tools so, in order to allow numerical computations, the Euclidean space-time is discretized on a hyper-cubic lattice $L = (L_x, L_y, L_z, L_t)$. The choice of the lattice spacing, usually denoted a , is arbitrary, but most often it is chosen to be equal for all dimensions. if we then define a lattice site $n = (n_x, n_y, n_z, n_t)$ where all the n s represent the coordinates of a point in the lattice Λ , our fields are constrained to have values on the points an instead of on a continuum space-time x^μ .

$$\phi(x) \xrightarrow{\text{discretization}} \phi(an) \quad (2.3)$$

2.1.1 The Harmonic Oscillator Example

Should I include this?

2.2 Discretization of QCD on the Lattice

In the case of QCD there are two types of field at play, the gluon gauge field A and the n_f fermionic quark fields ψ .

2.2.1 Naïve Discretization of Fermions

In this section the fermion discretization procedure found in [11] is followed, but also some elements from [12], quoting the main intermediate steps that lead to the formulation of Lattice QCD. The starting point is the fermionic euclidean action in the continuum:

$$S_F[\psi, \bar{\psi}] = \int dx^4 \bar{\psi}(x) (\gamma_\mu \partial^\mu + m) \psi(x) \quad (2.4)$$

now we discretize the euclidean space-time on a lattice Λ of spacing a , each point will be denoted with n . The partial derivative can be turned into the central finite difference between neighboring points along the direction of the derivative:

$$\partial_\mu \psi(x) \rightarrow \frac{\psi(n + \hat{\mu}) - \psi(n - \hat{\mu})}{2a} \quad (2.5)$$

The discretized fermion action is then:

$$S_F[\psi, \bar{\psi}] = a^4 \sum_{n \in \Lambda} \bar{\psi}(n) \left[\sum_{\mu=1}^4 \gamma_\mu \frac{\psi(n + \hat{\mu}) - \psi(n - \hat{\mu})}{2a} + m\psi(n) \right] \quad (2.6)$$

As we did in section 1.1.2 we try to apply a local gauge transformation $\Omega(n)$ to the field. It is simple to show that the terms of the derivative in the action are not gauge invariant:

$$\bar{\psi}(n)\psi(n \pm \hat{\mu}) \rightarrow \bar{\psi}(n)\Omega^\dagger(n)\Omega(n \pm \hat{\mu})\psi(n \pm \hat{\mu}) \quad (2.7)$$

The problem is in the way the derivative was discretized, it also removed one Lorentz index so it had to be wrong, and the solution is the introduction of an additional field as in 1.1.2 that has the correct transformation laws. This field must connect the values of the fermion field at two different lattice sites and because of this it is denoted "link variables" and by convention it is denoted as $U(n, n + \hat{\mu}) = U_\mu(n)$. Furthermore, it must depend on the orientation along the μ direction in a simple way:

$$U(n, n - \hat{\mu}) \equiv U_{-\mu}(n) = U_\mu(n - \hat{\mu})^\dagger \quad (2.8)$$

In particular, we want it to transform as:

$$\begin{aligned}\bar{\psi}(n)U_\mu(n)\psi(n + \hat{\mu}) &\rightarrow \bar{\psi}(n)\Omega^\dagger(n)U'_\mu(n)\Omega(n + \hat{\mu})\psi(n \pm \hat{\mu}) \\ \bar{\psi}(n)U_{-\mu}(n)\psi(n - \hat{\mu}) &\rightarrow \bar{\psi}(n)\Omega^\dagger(n)U'_{-\mu}(n)\Omega(n + \hat{\mu})\psi(n \pm \hat{\mu})\end{aligned}\quad (2.9)$$

from which we infer that:

$$\begin{aligned}U_\mu(n) &\rightarrow U'_\mu(n) = \Omega(n)U_\mu(n)\Omega^\dagger(n + \hat{\mu}) \\ U_{-\mu}(n) &\rightarrow U'_{-\mu}(n) = \Omega(n)U_{-\mu}(n)\Omega^\dagger(n - \hat{\mu})\end{aligned}\quad (2.10)$$

the field $U_\mu(n)$ which we identify with the link variables depends on the direction of the move along the μ direction. A visual representation is given in fig. 2.1,



Figure 2.1: Schematic representation of the link variables $U_\mu(n)$ and $U_{-\mu}(n)$ on the lattice.

With this results we can write a gauge invariant lattice fermion action as:

$$S_F[\psi, \bar{\psi}] = a^4 \sum_{n \in \Lambda} \bar{\psi}(n) \left[\sum_{\mu=1}^4 \gamma_\mu \frac{U_\mu(n)\psi(n + \hat{\mu}) - U_{-\mu}(n)\psi(n - \hat{\mu})}{2a} + m\psi(n) \right] \quad (2.11)$$

2.2.2 The Gauge Transporter and the Wilson Loop

A more formal definition of the link variables we can look at the gauge transporter. This is the path-ordered product, denoted with \mathcal{P} of a gauge field $A(x)$ along some curve \mathcal{C} between two points in space-time:

$$G(x, y) = \mathcal{P} \exp \left(i \int_x^y A(x') dx' \right) \quad (2.12)$$

An important thing to note now is that link variables belong to the gauge group, $SU(3)$ for QCD, and not to the algebra, $\mathfrak{su}(3)$. With this definition is easy to see the relation we just stated earlier on the direction change:

$$U(n, n - \hat{\mu}) = U_{-\mu}(n) = U_\mu^\dagger(n) \quad (2.13)$$

In the continuum case it can be shown, in [2] for example, that the trace of a gauge transporter that has the same start and final point, a Wilson Loop, is gauge invariant. On the lattice the minimal Wilson loop is just a square:

$$\begin{aligned}P_{\mu\nu}(n) &= U_\mu(n)U_\nu(n + \hat{\mu})U_{-\mu}(n + \hat{\mu} + \hat{\nu})U_{-\nu}(n + \hat{\nu}) \\ &= U_\mu(n)U_\nu(n + \hat{\mu})U_\mu^\dagger(n + \hat{\nu})U_\nu^\dagger(n)\end{aligned}\quad (2.14)$$

a pictorial representation is given in fig. 2.2.

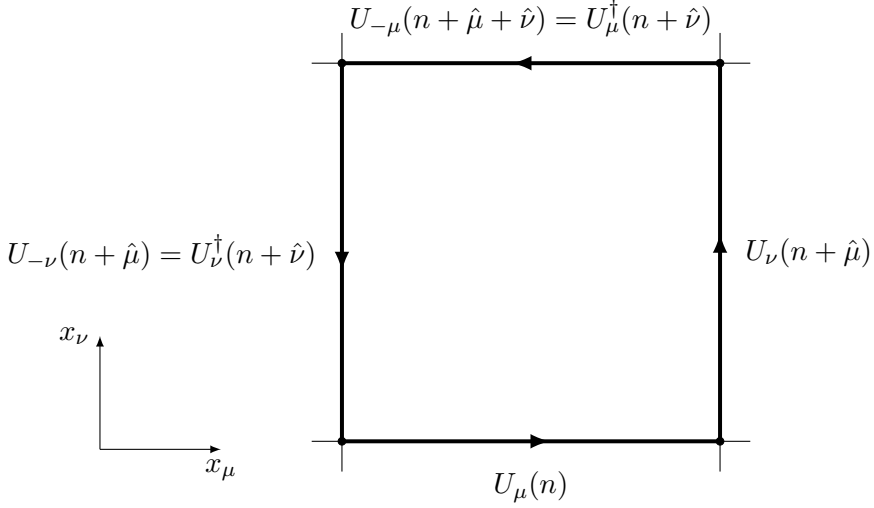


Figure 2.2: The Plaquette, as defined on the lattice, it terms of the oriented product of the link variables of a minimal square in the plane $\mu\nu$.

Up to order $\mathcal{O}(a)$ the integral on the straight line connecting two points on the lattice can be approximated with $aA_\mu(n)$, giving us $U_\mu(n) = \exp(iaA_\mu(n))$. This allows us to write using the Baker-Campbell-Hausdorff formula:

$$\begin{aligned} P_{\mu\nu}(n) &= \exp \left[iaA_\mu(n) + iaA_\nu(n + \hat{\mu}) - iaA_\mu(n + \hat{\nu}) - iaA_\nu^\dagger(n) - \frac{a^2}{2}[A_\mu(n), A_\mu(n + \hat{\mu})] \right. \\ &\quad \left. - \frac{a^2}{2}[A_\nu(n + \hat{\nu}), A_\nu(n)] + \frac{a^2}{2}[A_\mu(n), A_\nu(n)] + \frac{a^2}{2}[A_\nu(n + \hat{\mu}), A_\mu(n + \hat{\nu})] \right. \\ &\quad \left. + \frac{a^2}{2}[A_\mu(n), A_\mu(n + \hat{\nu})] + \frac{a^2}{2}[A_\nu(n + \hat{\mu}), A_\nu(n)] + \mathcal{O}(a^3) \right] \end{aligned} \quad (2.15)$$

Now the terms that are shifted from the site n are expanded as:

$$A_\mu(n + \hat{\nu}) = A_\mu(n) + a\partial_\nu A_\mu(n) + \mathcal{O}(a^2) \quad (2.16)$$

and with this substitution most terms cancel and we are left with:

$$\begin{aligned} P_{\mu\nu}(n) &= \exp [ia^2(\partial_\mu A_\nu(n) - \partial_\nu A_\mu(n) + i[A_\mu(n), A_\nu(n)]) + \mathcal{O}(a^3)] \\ &= \exp [ia^2 F_{\mu\nu}(n) + \mathcal{O}(a^3)] \end{aligned} \quad (2.17)$$

This term can be used to build the euclidean lattice action term for the gluons. In particular, we would like a term of the form:

$$S_G[U] = \frac{a^4}{2g^2} \sum_{n \in \Lambda} \sum_{\mu\nu} \text{Tr}(F_{\mu,\nu}(n)^2) \quad (2.18)$$

Up to order $\mathcal{O}(a^2)$ this can be obtained by:

$$S_G[U] = \frac{2}{g^2} \sum_{n \in \Lambda} \sum_{\mu < \nu} \Re \text{Tr}(\mathbb{1} - P_{\mu\nu}(n)) \quad (2.19)$$

Higher order corrections to this action can be computed analytically by considering higher orders in the BCH expansion and in the exponential expansion when constructing 2.19.

2.2.3 Lattice Fermions

The discretization of fermions as discussed in the previous section is incomplete. It becomes evident if one considers the Fourier transform of the propagator. Let's first rewrite 2.11 in a more compact way, introducing the lattice Dirac propagator $M_{xy}[U]$.

$$S_F[\psi, \bar{\psi}] = \sum_{n \in \Lambda} \bar{\psi}(x) M_{xy}[U] \psi(y) \quad (2.20)$$

with

$$M_{xy}[U] = \sum_{\mu=1}^4 \gamma_\mu \frac{U_\mu(x) \delta_{x,(y-\hat{\mu})} - U_{-\mu}^\dagger(x) \delta_{x,(y+\hat{\mu})}}{2a} + m \delta_{x,y} \quad (2.21)$$

in momentum space the propagator becomes:

$$\tilde{M}_{pq} = \delta(p - q) \tilde{M}(p) \quad : \quad \tilde{M}(p) = m \mathbf{1} + \frac{i}{a} \sum_{\mu=1}^4 \gamma_\mu \sin(p_\mu a) \quad (2.22)$$

In order to calculate the inverse of the propagator in real space we need to invert the one in momentum space and perform an inverse Fourier transform. However, the inverse of the propagator in Fourier space has multiple poles:

$$\tilde{M}(p)^{-1} \Big|_{m=0} = \frac{-ia \sum_\mu \gamma_\mu \sin(p_\mu a)}{\sum_\mu \sin^2(p_\mu a)} \quad (2.23)$$

the problem vanishes for $a \rightarrow 0$, the continuum case, returning just one fermion type, but on the lattice multiple fermions. This is known as the “doubling problem”. The solution, proposed by Wilson, is to modify the propagator adding some terms that make the poles in the inverse of the Fourier transformed propagator vanish. The final form of the Wilson Fermion Action is:

$$S_F[\psi, \bar{\psi}] = \sum_{n \in \Lambda} \bar{\psi}(x) M_{xy}^W[U] \psi(y) \quad (2.24)$$

with $m_{xy}^W[U]$ being the Wilson propagator:

$$M_{xy}^W[U] = \frac{1}{2a} \sum_{\mu=\pm 1}^{\pm 4} (\mathbf{1} - \gamma_\mu) U_\mu(x) \delta_{x,(y-\hat{\mu})} + \left(m + \frac{4}{a} \right) \delta_{x,y} \quad (2.25)$$

the shorthand notation $\gamma_{-\mu} = -\gamma_\mu$ has been introduced.

Now that all the needed information about the action and the fields is set, mainly through equations 2.11 and 2.24, the picture of how to discretize QCD from the continuum Minkovskian space-time to an euclidean space-time lattice.

2.3 Path Integrals on the Lattice

To express expectation values and correlators on the lattice, path integral formalism is used. The partition function, as we have seen earlier, is the path integral of the fields over the whole space of the action. For the case of QCD the fields are U , ψ and $\bar{\psi}$:

$$Z = \int \mathcal{D}\psi \mathcal{D}\bar{\psi} \mathcal{D}U e^{-S[\psi, \bar{\psi}, U]} \quad (2.26)$$

with the action being the sum of the gluonic and fermionic parts:

$$S[\psi, \bar{\psi}, U] = S_G[U] + S_F[\psi, \bar{\psi}, U] = S_G[U] + \sum_f \bar{\psi} M \psi \quad (2.27)$$

The immediate simplification is to integrate out the fermion fields. As in the continuum case one can perform an integration on the Grassmann-valued fields, in general for an integral over some Grassmann numbers θ_i and their complex conjugates θ_i^* , and a Hermitean matrix K :

$$\begin{aligned} \int \mathcal{D}\Theta^* \mathcal{D}\Theta e^{-\Theta K \Theta} &= \left(\prod_i \int d\theta_i^* d\theta_i \right) e^{-\theta_i^* K_{ij} \theta_j} = \left(\prod_i \int d\theta_i^* d\theta_i \right) e^{-\sum_i \theta_i^* k_i \theta_i} \\ &= \prod_i b_i = \det B \end{aligned} \quad (2.28)$$

This result is very different from what one would get in the real case, $(2\pi)^n / \det B$. It can also be shown that:

$$\begin{aligned} \int \mathcal{D}\Theta^* \mathcal{D}\Theta \theta_a^* \theta_b e^{-\Theta K \Theta} &= \left(\prod_i \int d\theta_i^* d\theta_i \right) \theta_a^* \theta_b e^{-\theta_i^* K_{ij} \theta_j} = \left(\prod_i \int d\theta_i^* d\theta_i \right) \theta_a^* \theta_b e^{-\sum_i \theta_i^* k_i \theta_i} \\ &= (\det B)(B^{-1})_{ab} \end{aligned} \quad (2.29)$$

This last result is crucial for computing fermion propagators for example, for a given “source” $\bar{\psi}(x)$ and a “sink” $\psi(y)$ the propagator between the two can be computed via path integrals, but it requires inverting the fermion action matrix.

With the result of 2.28 we can simplify greatly the partition function:

$$Z = \int \mathcal{D}\psi \mathcal{D}\bar{\psi} \mathcal{D}U e^{-S[\psi, \bar{\psi}, U]} = \int \mathcal{D}U e^{-S_G[U]} \det M[U] \quad (2.30)$$

In a similar fashion as in statistical mechanics, the expectation value of an observable on the lattice can be computed as:

$$\langle O \rangle = \frac{1}{Z} \int \mathcal{D}U O(\psi, \bar{\psi}, U) e^{-S_G[U]} \det M[U] \quad (2.31)$$

The above expression cannot be evaluated or simplified analytically any further, so the usual approach is to approximate the path integral numerically. The main idea is to create an ensemble

of field configurations to reproduce the integral $\int \mathcal{D}$, on such set $\mathcal{U} = \{U_1, U_2, \dots, U_N\}$ one computes the observable and the average value is the expectation value of the observable:

$$\langle O \rangle \approx \frac{1}{N} \sum_{i=1}^N O(\psi, \bar{\psi}, U_i) \quad (2.32)$$

The choice of the set \mathcal{U} is the interesting part, and it starts from identifying parts of 2.31 as a probability distribution, in particular, the probability of a configuration U is identified with:

$$P[U] = \frac{e^{-S_G[U]} \det M}{Z} \quad (2.33)$$

The integral is then evaluated using Monte Carlo integration, where the different configurations are chosen in the most widely accepted solution via a Markov chains. Given a field configuration U_i one chooses the following configuration U_{i+1} only based on properties of U_i . Later we will see how the Metropolis algorithm, one of the simplest Markov Chain Monte Carlo methods has been implemented.

2.3.1 Pure Gauge Field Theory

Computing full QCD on the lattice is computationally expensive, mainly due to the integration of fermions via the determinant. From a numerical point of view, the determinant need to be computed at every step of the Markov chain that is used to evaluate the path-integral and this operation affects the time cost of sampling the configuration space dramatically. A first approach is to neglect the determinant completely, considering it constant. This is effectively removing dynamical fermions, freezing them to the lattice sites. This approximation is usually referred to as “quenched QCD”, or QQCD. The properties of this theory, that is then reduced to a simple Yang-Mills theory are still interesting to study and have played historically a very important role, being the only accessible simulation until sufficient computing power became available.

2.3.2 Observables

On the lattice, given the transformation 2.10, any product of link variables that starts and end at the same lattice-site, a closed loop, is gauge invariant. The average values of these objects over the whole lattice can be linked to physical observables, for example the field tensor. In a more general form any observable $L[U]$ defined as

$$L[U] = \text{Tr} \left[\prod_{(n,\mu) \in \mathcal{L}} U_\mu(n) \right] \quad (2.34)$$

where \mathcal{L} is a closed loop of links on the lattice is a gauge invariant object and a candidate observable.

Plaquette

The simplest observable, which we have already encountered upon defining the Wilson action in 2.11, is the plaquette. This is the minimal closed loop on the lattice and its value is related to the coupling constant of the action. For each lattice site there are 12 possible plaquettes to be computed, given all the combinations of euclidean indeces. A proper definition of the observable is:

$$P[U] = \frac{1}{6|\Lambda|} \sum_{n \in \Lambda} \sum_{\mu < \nu} P_{\mu\nu}(n) \quad (2.35)$$

where $P_{\mu\nu}(n)$ is the one defined in eq. (2.15). As a side note, in actual calculations at every lattice site only the positive sign link variables are stored, so the second line of 2.15 is the one that is actually used in simulations.

Energy Density

The energy of the field is proportional to the square of the field tensor, in particular:

$$E[U] = -\frac{1}{4|\Lambda|} \Re \text{Tr}(G_{\mu\nu} G^{\mu\nu}) \quad (2.36)$$

In order to estimate this quantity, one has to compute the field tensor at every lattice site, square it and sum over the whole space. It is then usually normalized by the lattice volume (the number of sites), to get the density. The simplest definition of the field tensor is $G_{\mu\nu}^{(plaq)} = \mathbf{1} - P_{\mu\nu}$ but this is not very accurate. A more symmetric definition can be obtained by the “clover”, that is summing all the plaquettes of a same plane $\mu\nu$ that start from a given lattice site.

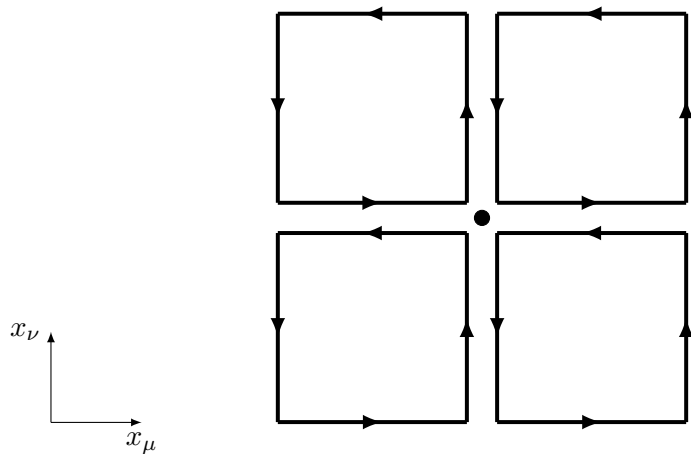


Figure 2.3: Schematic representation of the symmetric definition of the clover term $G_{\mu\nu}^{(clover)}$ on the lattice.

In terms of link variables this is equal to:

$$\begin{aligned} G_{\mu\nu}^{(clover)}(n) = & \frac{1}{4} \left[U_\mu(n)U_\nu(n + \hat{\mu})U_\mu^\dagger(n + \hat{\nu})U_\nu^\dagger(n) \right. \\ & - U_\nu(n)U_\mu^\dagger(n + \hat{\nu})U_\nu^\dagger(n - \hat{\mu})U_\mu(n - \hat{\mu}) \\ & + U_\mu^\dagger(n - \hat{\mu})U_\nu^\dagger(n - \hat{\mu} - \hat{\nu})U_\mu(n - \hat{\mu} - \hat{\nu})U_\nu(n - \hat{\nu}) \\ & \left. - U_\nu^\dagger(n - \hat{\nu})U_\mu(n - \hat{\nu})U_\nu(n + \hat{\mu} - \hat{\nu})U_\mu^\dagger(n) \right] \end{aligned} \quad (2.37)$$

Topological Charge

The gauge fields in QCD exhibit particular topological properties that are believed to have important physical implications [13][14]. The topological charge is an integer quantum number of the field in the continuum, but on the lattice certain definitions can be used to reproduce the continuum properties, especially for the so called “topological susceptibility”, that is the second moment of the distribution of the topological charge, which seems to be independent from the definitions of the base observable [15]. In the continuum topological sectors, regions of space with same charge, are separated from each other, on the lattice through discretization effects the behavior is different, with instantons that allow tunneling between sectors [16].

The topological charge is the integral over all space-time of the topological charge density:

$$Q = \int d^4x q(x) \quad (2.38)$$

where

$$q(x) = \frac{1}{64\pi^2} \text{Tr}(F_{\mu\nu}\tilde{F}^{\mu\nu}) \quad (2.39)$$

with $\tilde{F}^{\mu\nu} = \frac{1}{2}\epsilon^{\mu\nu\rho\sigma}F^{\rho\sigma}$. This can be estimated on the lattice, in the simplest way, by using the same definition of the field strength tensor we used before for the energy density, the clover:

$$Q[U] = \frac{1}{64\pi^2} \sum_{n \in \Lambda} \sum_{\mu < \nu} \epsilon^{\mu\nu\rho\sigma} \text{Tr}[G_{\mu\nu}^{(clover)}(n)G_{\rho\sigma}^{(clover)}(n)] \quad (2.40)$$

As the lattice spacing is reduced, approaching the continuum, the topological sectors get more and more separated, preventing tunneling between them. This makes the Markov chain used to generate the ensemble less efficient in terms of growing autocorrelation times, as will be shown in section 5.2.

A derived quantity of great interest is the topological susceptibility χ , that is proportional to the expectation value of the square of the topological charge:

$$\chi = \frac{(\hbar c)^4}{a^4 |\Lambda|} \langle Q^2 \rangle \quad (2.41)$$

This observable is particularly important for the properties of instantons on the lattice and its value can be related via the Witten-Veneziano formula to the mass of the η' .

2.4 Modern Lattice QCD Calculations

motlo vaga...

The state of the art calculations in Lattice QCD involve improved fermion and gluon actions. For the gluon sector the improvements are based on finding linear combinations of gauge invariant loops, such as 2×1 , 2×2 and 3×1 rectangles to systematically remove the higher order in the right-hand side of eq. (2.17). For fermions the improvements consist on actions that preserve certain symmetries more than others, like chiral fermion actions or staggered fermions. On the algorithm side, the currently most used method to generate gauge field configuration is the Hybrid Monte Carlo method, which combines stochastic sampling with hamiltonian dynamic updates in the gauge field space. Other interesting algorithmic problems regard the calculation of fermion determinants, which typically involve very large sparse matrix diagonalization. A fundamental concept in Lattice calculations is to recover the continuum limit in a controlled manner at the end of the analysis. The error sources that come into play when discretizing space-time on a fixed lattice are:

- Finite Volume Effects: caused by the non infinite domain of the simulation. Usually periodic boundary conditions are implemented to simulate infinite space, but one should always check if the total lattice volume is large enough, especially when dealing with large systems such as multiple baryons.
- State Isolation and Signal to Noise: when computing correlators between two points on the lattice it is possible to extract energy states of hadrons by looking at the exponential decay of the correlator in euclidean time. However this problem is largely affect by random noise making it hard to extract even the ground state most of the times; excited states are rarely considered.
- Chiral Limit: by which is intended the limit for which the masses of the quarks, and consequently of the computed hadrons, on the lattice approach the physical masses. One might question why this is even the case and that calculations should be performed at the physical masses only. However, the fermion propagator matrix becomes more and more sparse the lower the mass of the quark is, making the numerical algorithms that should diagonalize it slower to converge. The usual approach is to perform calculations on a set of pion masses (this is the usual reference for this problem) and afterwards the limit for $m_\pi^{(lat)} \rightarrow m_\pi^{(phys)}$ is taken to reproduce the physical observables.
- Continuum Limit: perhaps the most obvious thing to do to improve Lattice QCD calculations is to take finer and finer lattice spacings, to approach the continuum case. It should be noted however that this procedure has two downsides. First the lattice spacing in physical units is fixed by the quark masses, and as we previously mentioned, this affects the feasibility of the numerical simulation itself. Secondly, as the lattice approaches the continuum case the autocorrelation of observables in a given ensemble increases rapidly. This behavior, known as “critical slow-down” depends on the observable itself, some are more affected than others. The integrated autocorrelation time for the topological charge for example is believed to have either power-law with a large exponent or even an exponential relation to the lattice spacing.

As one can notice, Lattice QCD is still an open field of research in many aspects: the algorithmic/numerical, the extraction and improvement of the measurement of observables and the theoretical model itself.

Chapter 3

Advanced Topics in Lattice QCD

In this sections we will present some problems and methods that are used in Lattice QCD and in lattice Pure Gauge Theories. A 4-loop corrected expression for the β -function of QCD will be discussed as well, together with a tentative method of determining the scale parameter Λ from lattice caluclations.

3.1 Scale Setting in the Quenched Approximation

On the lattice quantities are defined to be dimensionless and in order to link them with physical observables they need to be fixed by multiplying them with the lattice spacing a to reproduce the physical units. The fundamental question is then how to connect the lattice spacing to the coupling used in the gluonic action.

In 1993 R. Sommer proposed to use the static quark potential as a reference in the case of $SU(2)$ theory [17]. Later in another work [18] a length scale r_0 was suggested for $SU(3)$ Yang-Mills theory to be set as the distance such that

$$r_0^2 F(r_0) = 1.65 \quad (3.1)$$

with $F(r_0)$ being the force between external static charges. In [18] also a parametrization of the ratio a/r_0 is provided, in terms of the coefficients of the renormalization group equation. To leading order one finds:

$$\frac{a}{r_0} \propto e^{-\frac{\beta}{12b_0}} \quad (3.2)$$

with inverse coupling $\beta = 6/g_0^2$ and b_0 the one loop coefficient of the perturbative expansion of the β function, see section 1.2.1 , $b_0 = 11/(4\pi)^2$. Using the ansatz:

$$\ln \left(\frac{a}{r_0} \right) = \sum_{k=0}^p a_k (\beta - 6)^k \quad (3.3)$$

a parametrization up to $p = 3$ has been fitted to data. The resulting interpolating function is:

$$\ln \left(\frac{a}{r_0} \right) = -1.6805 - 1.7139(\beta - 6) + 0.8155(\beta - 6)^2 - 0.6667(\beta - 6)^3 \quad (3.4)$$

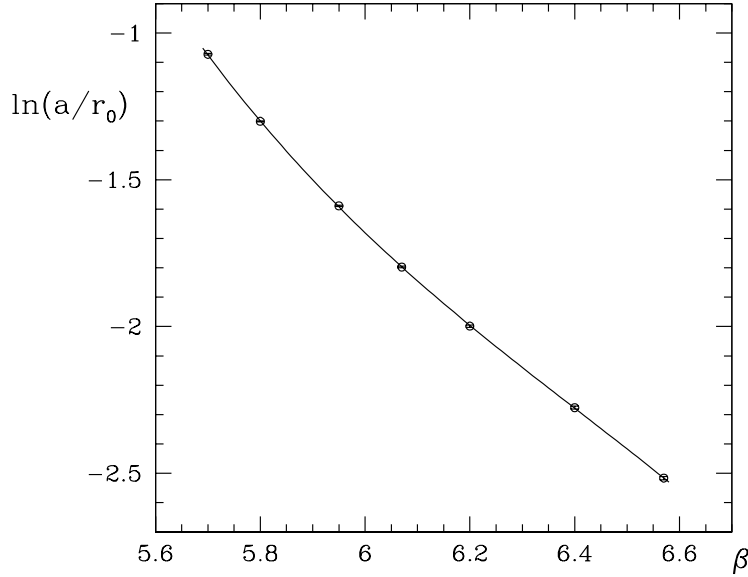


Figure 3.1: Data and interpolating function for $\ln(a/r_0)$ as found in [18].

This scale fixing procedure requires a proper estimate of the length scale from measurements of the static quark potential for various quark sources, which can be an expensive calculation at times. Often it is custom to set the length scale to a fixed value, namely $r_0 = 0.5$ fm, commonly called the Sommer scale parameter, and then use eq. (3.4) to extract a .

More recently another procedure to fix the energy scale has been proposed, based on the Gradient Flow Method, which will be discussed in section 3.3.1. The key idea is again to choose and observable that is lattice spacing independent. By choosing an arbitrary value for it one can use the observable as a reference scale for further calculations.

3.2 The Gradient Flow Method

The Gradient Flow Method, also known as the Wilson Flow in the case of QCD, is a method for studying non-linear quantum field theories by the properties of flows in the field space. The key idea is to see how the theory evolves as it becomes less local, by driving it to the stationary points of the action, applying a “diffusion-like” differential equation to the field in a fictitious dimension called “flow-time”.

For the $SU(3)$ gauge field case most of the theoretical foundation was set by M.Lüscher in [19][20] and for QCD in [21]. Starting from a field $A_\mu(x)$ the characterizing equations are:

$$\begin{aligned} \partial_{t_f} B_\mu &= D_\mu G_{\mu\nu} \\ G_{\mu\nu} &= \partial_\mu B_\nu - \partial_\nu B_\mu + [B_\mu, B_\nu] \end{aligned} \tag{3.5}$$

where the $B(t_f, x)$ field is the flowed version of the original field at flow-time t_f . This is imposed by fixing:

$$B_\mu|_{t_f=0} = A_\mu \tag{3.6}$$

The covariant derivative is extended to represent the derivative of the field B instead of A , this leaves the simple definition for the non-flowed field from the boundary condition. It is generalized straightforwardly as:

$$D_\mu = \partial_\mu + [B_\mu, \cdot] \quad (3.7)$$

In a discretized theory taking the derivatives is not a trivial procedure, but we can use instead the intuitive idea of the flow equations, that is to use the steepest descent method on the action of a field. We then introduce the flowed lattice gauge field $V_{t_f}(x, \mu)$ as the flowed version of a field $U(x, \mu)$. Our flow equation then becomes:

$$\partial_{t_f} V_{t_f}(x, \mu) = -g_0^2 [\partial_{x,\mu} S_G(V_{t_f})] V_{t_f}(x, \mu) \quad (3.8)$$

where S_G is the Wilson action, as defined in eq. (2.19), generalized to flowed fields. The generalization is really straightforward, as it only requires to compute the Wilson loops on the flowed gauge field.

The flow equations for the fermion fields, although they have not been used in this work, are:

$$\begin{aligned} \partial_{t_f} \chi &= \Delta \chi, & \partial_{t_f} \bar{\chi} &= \bar{\chi} \overleftarrow{\Delta} \\ \Delta &= D_\mu D_\mu, & D_\mu &= \partial_\mu + b_\mu \end{aligned} \quad (3.9)$$

note that Δ is the covariant laplacian in this notation. The initial conditions are naturally

$$\chi|_{t_f=0} = \psi, \quad \bar{\chi}|_{t_f=0} = \bar{\psi}, \quad (3.10)$$

3.3 Perturbative Analysis of the Wilson Flow

An important thing to consider when applying the Wilson flow to a field is the renormalization of the observables: one has to check that expectation values of observables at non-zero flow-time are renormalized quantities. Following the calculations performed in [19], we will consider the energy as our base observable.

First, we note that the flow equation is invariant under flow-time independent gauge transformations, this prevents a detailed study of the renormalization. So we consider a modified version of the flow equation by adding one term:

$$\partial_{t_f} B_\mu = D_\mu G_{\mu\nu} + \lambda D_\mu \partial_\nu B_\nu \quad (3.11)$$

the original case is obtained again by setting $\lambda = 0$ and considering:

$$B_\mu = \Lambda B_\mu|_{\lambda=0} \Lambda^{-1} + \Lambda \partial_\mu \Lambda^{-1} \quad (3.12)$$

and with $\Lambda(t, x)$ now being a flow-time dependent gauge transformation, set by:

$$\partial_{t_f} \Lambda_\mu = -\lambda \partial_\nu B_\nu \Lambda \quad \text{with } \Lambda|_{t_f=0} = 1 \quad (3.13)$$

The energy E as defined in eq. (2.36) is a gauge invariant object. One can observe that the modified flow equation is invariant under gauge transformations, hence the energy, as any other gauge invariant observable, will preserve their invariance. Using this modified flow equation it

is possible to write the expectation value of the energy as a function of the flow-time and of the renormalized coupling:

$$\langle E \rangle = \frac{3(N^2 - 1)g_0^2}{128\pi^2 t_f^2} [1 + \bar{c}_1 g_0^2 + \mathcal{O}(g_0^4)] \quad (3.14)$$

with:

$$\bar{c}_1 = \frac{1}{16\pi^2} \left[N \left(\frac{11}{3}L + \frac{52}{9} - 3\ln 3 \right) - N_f \left(\frac{2}{3}L + \frac{4}{9} - \frac{4}{3}\ln 2 \right) \right] \quad (3.15)$$

The equation is for general N , the gauge group dimension, and number of quark flavors N_f . The coefficient \bar{c}_1 is in terms of a scale $L = \ln(8\mu^2 t_f) + \gamma_E$ where μ is the renormalization energy scale and γ_E Euler's constant. From this last relation we can set a flow energy scale as $q = 1/\sqrt{8t_f}$ and give a definition of eq. (3.14) in terms of the running coupling $\alpha_s(q) = \frac{g_0^2}{4\pi}$:

$$\langle E \rangle = \frac{3(N^2 - 1)}{32\pi t_f^2} \alpha_s(q) [1 + k_1 \alpha_s(q) + \mathcal{O}(\alpha_s^2)] \quad (3.16)$$

where the coefficient k_1 is now:

$$k_1 = \frac{1}{4\pi} \left[N \left(\frac{11}{3}\gamma_E + \frac{52}{9} - 3\ln 3 \right) - N_f \left(\frac{2}{3}\gamma_E + \frac{4}{9} - \frac{4}{3}\ln 2 \right) \right] \quad (3.17)$$

In the case of $SU(3)$ symmetry group we have:

$$\langle E \rangle = \frac{3}{4\pi t_f^2} \alpha_s(q) [1 + k_1 \alpha_s(q) + \mathcal{O}(\alpha_s^2)], \quad k_1 = 1.0978 + 0.0075 \times N_f \quad (3.18)$$

The perturbative expansion is only valid for large values of q , that is when the flow-time is small. We also can notice that $\sqrt{8t_f}$ is the inverse of an energy, or a length. This gives us an intuitive picture of what the gradient flow does, that is to smear the field over a hyper-sphere of radius $\sqrt{8t_f}$. The gradient flow is the particularly interesting to study quantities that are divergent on the lattice because of discretization effects, like the topological susceptibility, which become smooth at non-zero t_f . In fig. 3.2 an example of the smearing effect of the gradient flow on the topological charge. The topological charge at $\sqrt{8t_f} = 0$ is highly affected by large fluctuations over the lattice sites. This for example affects the topological susceptibility as it is divergent. One can notice that the action of the flow equation is to remove such low distance fluctuations that at $\sqrt{8t_f} = 0$ fm are almost completely gone. For larger smearing radii the emergence of frozen well separated topological sectors becomes visible.

3.3.1 Scale Fixing with the Gradient Flow

Because of the smearing properties of the flow equation the fields are driven towards the minima of the action, which are in general independent from the lattice spacing. One can therefore set, for sufficiently large flow-times, decide to use the value of $t^2 \langle E \rangle$ to fix the scale of the lattice. This follows naturally from eq. (7.3) as once t^2 is moved to the left hand side only a function of the energy, expressed in terms of $\alpha_s(q)$ remains on the right hand side.

It has been proposed by Lüscher that a value of $t^2 \langle E \rangle = 0.3$ is large enough to be used as a reference scale. In fig. 3.3 we can indeed observe that the value is constant as a function of the lattice spacing (computed instead using the Sommer parameter).

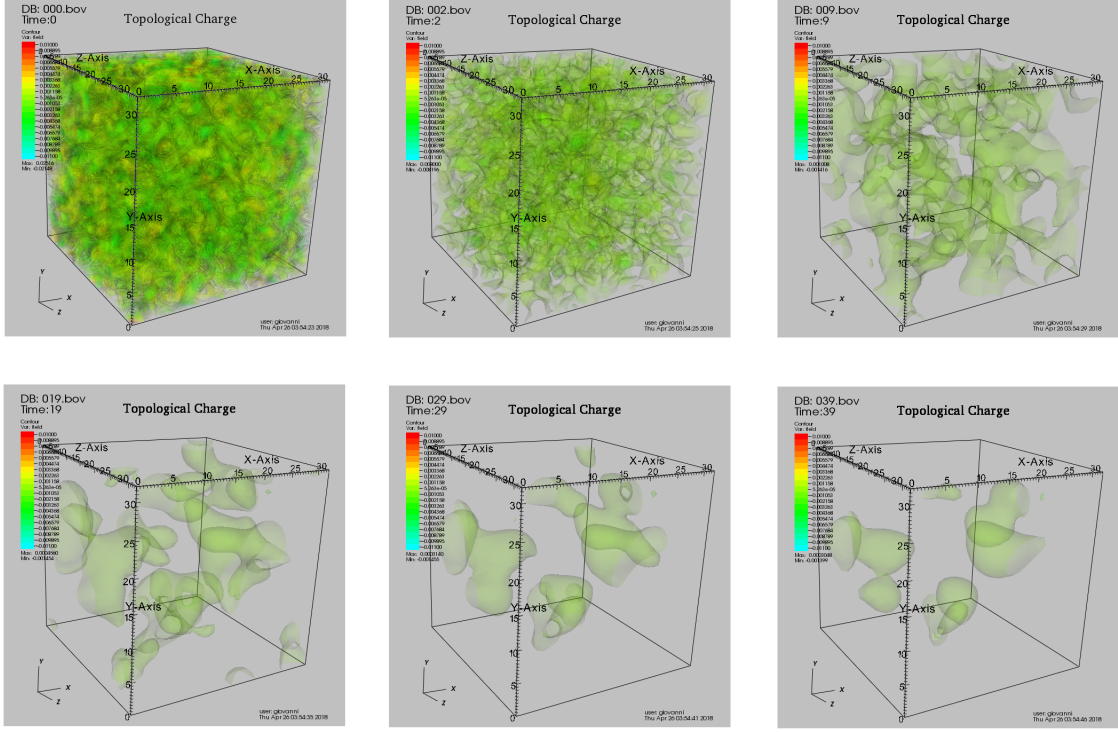


Figure 3.2: Topological charge computed ad one euclidean time of a lattice of size $32^3 \times 64$ with lattice spacing 0.06793 fm. The flow different plots are for flow-times $\sqrt{8t_f} = 0, 0.14, 0.30$ fm on the first row and $\sqrt{8t_f} = 0.43, 0.52, 0.60$ fm on the second row.

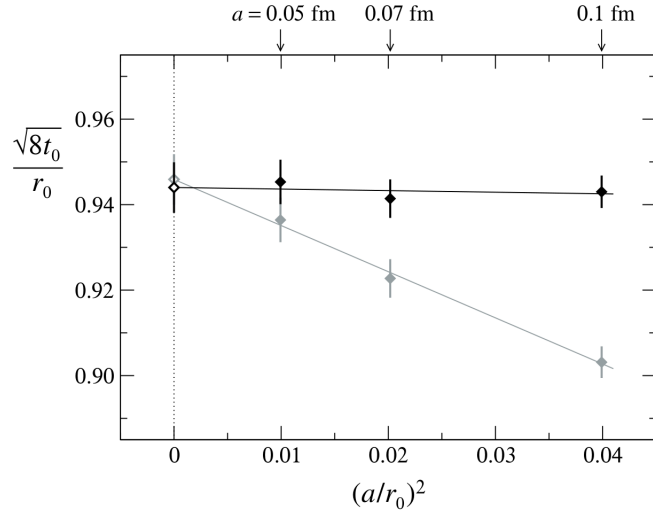


Figure 3.3: Plot of $\sqrt{8t_0}/r_0$ where t_0 is the value such that $t_0^2\langle E \rangle = 0.3$ for different lattice spacings taken from [22].

3.4 Estimating the Scale Parameter

Finally all the theoretical concepts and tools have been defined to state the main purpose of this work in a formal way. The main goal is to use the perturbative expression of the energy as a function of the flow-time and of the running coupling to estimate the scale parameter Λ . Since the code base that has been developed only for pure gauge theory, we will restrict the analysis for $N_f = 0$ for now, but in a future work the more interesting determination of Λ_{QCD} could be performed the same way.

On the lattice the quantity $t_f^2 \langle E \rangle$ can be computed easily, this leaves only the coupling on the right hand side of eq. (7.3) as the unknown variable. One can then choose an order for the expansion of the Renormalization Group Equation:

$$\mu^2 \frac{d\alpha(\mu)}{d\mu^2} = \beta(\alpha) = -(b_0\alpha^2 + b_1\alpha^3 + \dots) \quad (3.19)$$

When solving the equation for $\alpha(\mu)$ there is some freedom on the choice of the renormalization point, as we have seen in eq. (1.20), such that the equation in the end can be simplified by the introduction of a scale parameter.

Using the data computed on the lattice, by first taking the continuum limit in order to account for discretization effects, estimate the scale parameter.

3.4.1 4-loop Corrected Running Coupling

The equation needs to be solved for $\alpha(\mu)$ and a convenient approximate form, correct up to order 4, that is including 4-loop diagrams in the calculations, parametrized by 4 coefficients can be found in [23]:

$$\alpha(\mu) = \frac{1}{b_0 t} \left[1 - \frac{b_1 \ln t}{b_0 t} + \frac{b_1^2 (\ln^2 t - \ln t - 1) + b_0 b_2}{b_0^4 t^2} - \frac{b_1^3 (\ln^3 t - \frac{5}{2} \ln^2 t - 2 \ln t + \frac{1}{2}) + 3b_0 b_1 b_2 \ln t - \frac{1}{2} b_0^2 b_3}{b_0^6 t^3} \right] \quad (3.20)$$

there the convenient notation of $t \equiv \ln \frac{\mu^2}{\Lambda^2}$ has been introduced. The coefficients b_0, b_1, b_2 and b_3 can be computed analytically for a general theory on $SU(3)$ with N_f quark flavors. While b_0 and b_1 have known exact values, the other two parameters are renormalization scheme dependent,

and we chose the ones computed in the \overline{MS} found in [24]. The coefficients are then:

$$\begin{aligned} b_0 &= \frac{1}{(4\pi)} \left[11 - \frac{2}{3} N_f \right] \\ b_1 &= \frac{1}{(4\pi)^2} \left[102 - \frac{38}{3} N_f \right] \\ b_2 &= \frac{1}{(4\pi)^3} \left[\frac{2857}{2} - \frac{5033}{18} N_f + \frac{325}{54} N_f^2 \right] \\ b_3 &= \frac{1}{(4\pi)^4} \left[\left(\frac{149753}{6} + 3564\zeta_3 \right) - \left(\frac{1078361}{162} + \frac{6508}{27}\zeta_3 \right) N_f \right. \\ &\quad \left. + \left(\frac{50065}{162} + \frac{6472}{81}\zeta_3 \right) N_f^2 + \frac{1093}{729} N_f^3 \right] \end{aligned} \tag{3.21}$$

or in a numerical form, substituting also the Riemann zeta-function value $\zeta_3 = 1.202056903\dots$ one gets the more handy expression

$$\begin{aligned} b_0 &\approx \frac{1}{(4\pi)} (11 - 0.66667 N_f) \\ b_1 &\approx \frac{1}{(4\pi)^2} (102 - 12.66667 N_f) \\ b_2 &\approx \frac{1}{(4\pi)^3} (1428.50 - 279.611 N_f + 6.01852 N_f^2) \\ b_3 &\approx \frac{1}{(4\pi)^4} (29243.0 - 6946.30 N_f + 405.089 N_f^2 + 1.49931 N_f^3) \end{aligned} \tag{3.22}$$

with the aid of these coefficients the only unknown variable in eq. (1.20) is the scale parameter, so by fitting this function to the lattice over a range of energies where some degree of overlap is found leads to an estimation of Λ .

Part II

Implementation

Chapter 4

Designing a Lattice $SU(3)$ Yang-Mills Theory Code

One of the major focuses of this work has been a completely new implementation of a program to generate and analyze $SU(3)$ gauge fields. As it is common practice in Lattice QCD numerical implementations, the program is separated in two parts that are computationally intensive and one that is easier in that sense:

- *generation of gauge fields*: in this case it is done through a simple Metropolis algorithm using the standard Wilson action;
- *computation of observables*: this includes applying the gradient flow as well as computing the energy density and the topological charge at every flow-time;
- *computation of derived observables*: mainly post analysis, error analysis and model fits to data.

Here we will present the main features of the first two steps, which are the most interesting ones. The programming language of choice is C++because of its high efficiency, high abstraction capabilities (the code-base is highly object oriented) and for the easiness of the MPIintegration. The analysis of data has been performed using python and in particular relying heavily on its standard data science packages such as numpy and pandas.

4.1 Generating Pure Gauge Fields

The task of generating lattice field configurations is extremely demanding in terms of computation requirements. The case of QCD is much more demanding than that of a pure Yang-mills theory, but overall the latter calculation is still challenging. The main, and perhaps overwhelmingly simple, reason for this problem is the dimensionality. Dealing with a discretized space-time

lattice, things tend to scale with powers of 2^4 , a trivial example is cutting in half the lattice spacing keeping a fixed total volume: this requires 16 more points in the global lattice.

To get a better feeling of the algorithm we first have to look at what the basic object of the program is: the lattice. The number of double precision floating point numbers to be stored for a field configuration is given by

$$\underbrace{N^3}_{\text{spatial dimension}} \times \underbrace{N_t}_{\text{time dimension}} \times \underbrace{4}_{\text{links per site}} \times \underbrace{9}_{\text{SU(3) matrix size}} \times \underbrace{2}_{\text{real and imaginary part}} \quad (4.1)$$

this implies that, for example, if we choose $N = 48$, $N_t = 96$ the resulting configuration is 6115295232 *bytes* large, that is 5.7 *GBytes*. This limits greatly the possibility of simulating large systems

The basic element at each lattice site is a set of 4 different $SU(3)$ matrices, one for each dimension. These links are to be intended as the integral of the gauge field from one site to the adjacent one along each dimension. A more formal description has been given in chapter 3.

4.1.1 The Metropolis Algorithm

The main algorithm that has been used to generate an ensemble of gauge field configurations is the Metropolis Algorithm. It is a widely popular Markov Chain Monte Carlo Method to generate a sequence of random samples from a probability distribution [25].

In general, a Markov Chain is a sequence randomly chosen variables X_1, X_2, \dots, X_t , in our case a lattice field configuration, with the Markov Property: that is the probability of the step $t + 1$ depends only on the variable X_t :

$$P(X_{t+1} = x | X_1 = x_1, X_2 = x_2, \dots, X_t = x_t) = P(X_{t+1} = x | X_t = x_t) \quad (4.2)$$

In the case where the probabilities of moving from a state $X_i = i$ to a state $X_j = j$ is not known, the transition probability from the two states, $W(i \rightarrow j)$ can be split into two contributions: the probability $T(i \rightarrow j)$ for making the transition to state j being in state i and the probability of accepting this transition $A(i \rightarrow j)$.

$$W(i \rightarrow j) = A(i \rightarrow j)T(i \rightarrow j) \quad (4.3)$$

if a Probability Distribution Function (PDF) is known for the process, we can label the probability of a given state at a fixed time $w_i(t)$. The transition probability to a state j at time $t + 1$ is the sum of the transition probabilities of moving to state j from state i plus the probability of being in state i at time t and rejecting to move to any other state:

$$\begin{aligned} w_j(t+1) &= \sum_i [w_i(t)T(i \rightarrow j)A(i \rightarrow j) + w_j(t)T(j \rightarrow i)(1 - A(j \rightarrow i))] \\ &= w_j(t) + \sum_i [w_i(t)T(i \rightarrow j)A(i \rightarrow j) - w_j(t)T(j \rightarrow i)A(j \rightarrow i)] \end{aligned} \quad (4.4)$$

for large t , when the equilibrium is reached, we require that $w_j(t+1) = w_j(t) = w_j$, and thus we have:

$$\sum_i w_i T(i \rightarrow j) A(i \rightarrow j) = \sum_i w_j T(j \rightarrow i) A(j \rightarrow i) \quad (4.5)$$

now, considering that the transition probability from a state j to all other states must be normalized $\sum_i W(j \rightarrow i) = \sum_i T(j \rightarrow i)A(j \rightarrow i) = 1$ we get:

$$\sum_i w_i T(i \rightarrow j) A(i \rightarrow j) = w_j \quad (4.6)$$

At this point, the further constrain of Detailed Balance is introduced, that is:

$$w_i W(i \rightarrow j) = w_j W(j \rightarrow i) \quad (4.7)$$

at equilibrium we then have:

$$\frac{w_i}{w_j} = \frac{W(i \rightarrow j)}{W(j \rightarrow i)} = \frac{T(i \rightarrow j)A(i \rightarrow j)}{T(j \rightarrow i)A(j \rightarrow i)} \quad (4.8)$$

Making the approximation that the transition probability between states is the same, $T(i \rightarrow j) = T(j \rightarrow i)$, the brute-force approach, we are left with the acceptance ratio of a move to a new state to be the ratio of the PDFs.

In our case the probability distribution of the gauge field configurations, labeled U is:

$$P(U) = \frac{e^{S_G[U]}}{Z} = \frac{e^{S_G[U]}}{\int \mathcal{D} U e^{S_G[U]}} \quad (4.9)$$

that is the exponential of gluon Wilson Action over the path integral of the same quantity over all space, the partition function. Luckily, we only need ratios of this quantity so the normalization part is not to be ever computed. We can rewrite any expectation value of an operator on the lattice as:

$$\langle O \rangle = \frac{\int \mathcal{D} U O[U] e^{S_G[U]}}{\int \mathcal{D} U e^{S_G[U]}} = \int \mathcal{D} U P(U) O[U] \quad (4.10)$$

which numerically becomes:

$$\langle O \rangle \approx \frac{1}{N} \sum_{i=1}^N O(U_i) \quad (4.11)$$

where, as described in section section 2.3 U_i is a set of configurations chosen with the PDF in eq. (4.9).

Noting that, since we only care about ratios in the PDF and that the PDF is an exponential, a huge simplification is to modify an initial guess for a field configuration only locally and check the local action difference. A simplified version of the algorithm is described below:

The actual implementation of this algorithm on discretized space-time is however not as trivial as it seems, because we are dealing with a lattice gauge configuration, so we need to define what is a random move and what is the action difference for our specific case.

One configuration is saved, in the form of a simple binary containing all the data of the lattice, as an intermediate result every N_C Monte Carlo updates. We need this in order to apply the gradient flow afterwards to the configurations and compute the observables we want. The choice of N_C turned out to be crucial for the autocorrelation of some observables, in particular the topological charge.

Algorithm 1 Metropolis Algorithm

```

1: configuration  $\leftarrow$  initial configuration
2: for  $i < MonteCarloCycles$  do
3:   for  $U$  in Lattice do
4:     newConfiguration  $\leftarrow$  randomMove( $U$ ) + configuration
5:      $\Delta S \leftarrow$  action(newConfiguration) – action(configuration)
6:     if  $\Delta S > \text{random}(0, 1)$  then
7:       configuration  $\leftarrow$  newConfiguration

```

4.1.2 Sampling the Configuration Space

To use Metropolis' algorithm we need to define what a random move is. Using the Wilson Action eq. (2.11), which is defined on plaquettes, an update on a single link variable can be seen as a small unitary transformation. In order to generate such transformation use three random $SU(2)$ matrices "close to unity". By this expression we mean that the real diagonal components are the dominant terms of the matrix. A recipe for generating these matrices is found in [11].

$$R_2 = \begin{pmatrix} r_{11} & r_{12} \\ r_{21} & r_{22} \end{pmatrix} \quad S_2 = \begin{pmatrix} s_{11} & s_{12} \\ s_{21} & s_{22} \end{pmatrix} \quad T_2 = \begin{pmatrix} t_{11} & t_{12} \\ t_{21} & t_{22} \end{pmatrix} \quad (4.12)$$

The elements of the matrix are chosen at random by choosing four random numbers r_0 , \mathbf{r} (a three component vector) between $(-\frac{1}{2}, \frac{1}{2})$. We then introduce a "spread parameter" ϵ that controls how much the off-diagonal terms will weight, so we scale our random variables by:

$$x_0 = \text{sign}(r_0)\sqrt{1 - \epsilon^2} \quad \mathbf{x} = \epsilon \frac{\mathbf{r}}{|\mathbf{r}|} \quad (4.13)$$

and we use these coefficients together with the generators of the $SU(2)$ group (the Pauli matrices) to build an element of the group:

$$U = x_0 \mathbb{1} + i\mathbf{x} \cdot \boldsymbol{\sigma} = \begin{pmatrix} u_{11} & u_{12} \\ u_{21} & u_{22} \end{pmatrix} \quad (4.14)$$

We then embed these $SU(2)$ matrices in three $SU(3)$ matrices by mapping them as:

$$R = \begin{pmatrix} r_{11} & r_{12} & 0 \\ r_{21} & r_{22} & 0 \\ 0 & 0 & 1 \end{pmatrix} \quad S = \begin{pmatrix} s_{11} & 0 & s_{12} \\ 0 & 1 & 0 \\ s_{21} & 0 & s_{22} \end{pmatrix} \quad T = \begin{pmatrix} 1 & 0 & 0 \\ 0 & t_{11} & t_{12} \\ 0 & t_{21} & t_{22} \end{pmatrix} \quad (4.15)$$

These three matrices are clearly members of $SU(3)$ and so is their product $X = RST$. We thus have defined a recipe for numerically generating random group transformations, the key element for our algorithm.

An additional element that we need to define is the action difference ΔS . On a single link $U_\mu(x)$ we apply a random transformation X and get $U'_\mu(x) = XU_\mu(x)$. The total change in the action

only depends on those plaquettes that contain the considered link variable. In four dimensions there are 12 such elements:

$$\Delta S = S[U'_\mu(x)] - S[U_\mu(x)] = -\frac{\beta}{N} \Re \operatorname{Tr}[U'_\mu(x) - U_\mu(x)]A \quad (4.16)$$

where A is the sum of the "staples" of the link U . They are the constant three sides of the plaquettes that contain U :

$$A = \sum_{\nu \neq \mu} \left[U_\nu(x + \mu)U_{-\mu}(x + \mu + \nu)U_{-\nu}(x + \nu) \right. \\ \left. + U_{-\nu}(x + \mu)U_{-\mu}(x + \mu - \nu)U_\nu(x - \nu) \right] \quad (4.17)$$

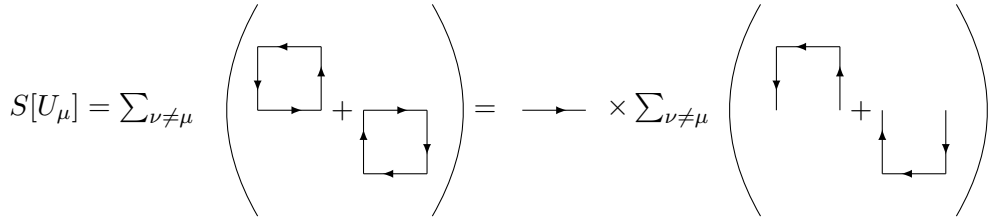


Figure 4.1: Schematic representation of the symmetric definition of action $S[U_\mu]$ expressed as a function of the staples .

4.1.3 Updates Strategies

There is now some arbitrariness in what is defined as an update. In this work we call an update the following procedure:

Algorithm 2 Metropolis Update

```

1: for  $x, \mu$  do
2:    $A \leftarrow \text{computeStaples}(x, \mu)$ 
3:   for  $i < N_H$  do
4:      $U_{\text{new}}(x, \mu) \leftarrow X \cdot U(x, \mu)$ 
5:      $\Delta S \leftarrow (U_{\text{new}}(x, \mu) - U(x, \mu)) \cdot A$ 
6:     if  $\text{realTrace}(\Delta S) > \text{random}(0, 1)$  then
7:        $U(x, \mu) \leftarrow U_{\text{new}}(x, \mu)$ 

```

These updates are the ones we consider when we refer to Monte Carlo cycles, autocorrelation times and so on. Note that each update includes a loop over all links on the lattice and that every link is "hit" N_H times before moving to the next one. This is done for computational efficiency, because computing the staples is the most expensive part of the algorithm, once A is computed for a link, the result is used to attempt multiple updates on the link. It can also be shown that if N_H is sufficiently large the algorithm becomes equivalent to the heatbath algorithm.

The order in which the links in the lattice are visited is also arbitrary. The simplest way, the ordered one, was adopted. This however might have impacted the autocorrelation of the system, not allowing significant modification to the system as an update depends on the neighbors. An alternative choice is a checkerboard pattern, which has potential benefits to the autocorrelation time of the observables as well as on the parallelization scheme ??.

4.1.4 Parallelization Scheme

Given the size of the lattice (from $V \approx 10^5$ to $V \approx 10^7$, the total number of lattice sites), it is necessary to split the computation of the updates on more than one processors. The most direct way is to divide the lattice into sub-blocks and have each process handle its portion of the field alone.

In an operative way, given a lattice of size (n_x, n_y, n_z, n_t) each space-time dimension is split into even portions, of size (s_x, s_y, s_z, s_t) and mapped on N_{procs} processors, having that:

$$N_{procs} = \frac{s_x}{n_x} \times \frac{s_y}{n_y} \times \frac{s_z}{n_z} \times \frac{s_t}{n_t} \quad (4.18)$$

A unique mapping can be performed from the “local” coordinates of the sub-block and the unique identifier of the processor that is given by the parallelization library. This way one can manage the distribution of the total lattice into N_{procs} sub-lattices. The usual periodic boundary conditions that are used in the calculations are changed into periodic communication patterns between the processors.

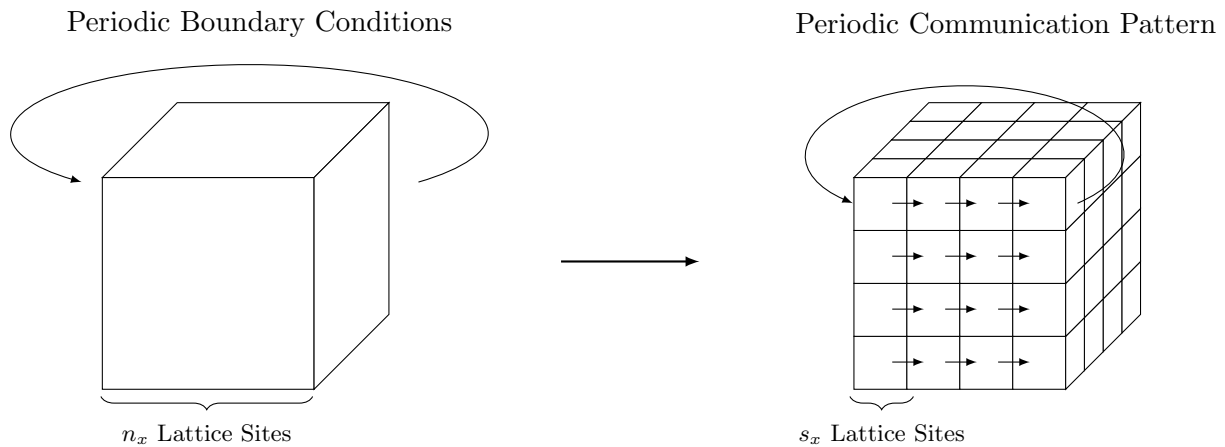


Figure 4.2: Schematic representation, in just 3 dimensions, of the splitting of the lattice into sub-lattices.

However, because of the dependence of the action difference of a link on its neighbors, when updating a link on the edge of a sub-block information about another block is needed. Here is where the Message Passing Interface (MPI) comes in use. For this particular problem we decided to use a point to point communication scheme between the processors, the use of periodic boundary conditions allowed also for non-blocking communications to be used, in particular the collective geometry based scheme shown in section 4.1.4 has been implemented.

When computing the staples, two links need to be fetched from the neighbor in the positive direction and, since all processors are synchronized, at the same time two links are requested from the neighbor in the negative direction. The `SendRecv` function of MPI is exactly what is needed.

Note that the communication is relevant only for the computation of the staples, this is another argument in favor of performing multiple hits on a link at every update. It is clear to see that the algorithm can be affected by large communication overhead problems. If the sub-blocks are too small, then most of the time would be spent on sending and receiving links from the neighbors. This causes the execution time to depend not linearly on the number of processors, instead the relation flattens at some value given by the communication overhead.

4.1.5 Summary of the Parameters

In total the algorithm needs four parameters as inputs. Of these, only one defines the physics of the system, the others have to be set and optimized in order to improve the acceptance ratio of the metropolis test and the autocorrelation of the observables computed on the generated configurations.

Parameter	Description
β	Coupling parameter of the Wilson Action
ϵ	"Spread" of the random $SU(3)$ elements for the updates
N_C	Number of updates between one saved configuration (observable measurement)
N_H	Number of of "hits" per link at every update, with constant staple

Table 4.1: Parameters for the Monte Carlo generation of Yang-Mills gauge field configurations via the Metropolis Algorithm

4.2 Wilson Flow of Gauge Configurations

To study the flow-time dependence of the observables a numeric implementation of eq. (3.8) is needed. The main challenge that this problem poses is how to numerically integrate the flow equation on the lattice, because it is important to preserve the $SU(3)$ Lie Group structure of the field through the numerical procedure. The problem is solved by using the so called Structure-Preserving Runge-Kutta Methods, in particular the Runge-Kutta Munthe-Kaas method that is designed to integrate first order ODE on a manifold [26, 27, 28]. The problem can be defined in a more general manner as:

$$\dot{V}_t = Z(V_t)V_t \quad (4.19)$$

here V_t is an element of a Lie group \mathcal{G} and $Z(V_t)$ is a function with values in the associated algebra \mathfrak{g} . The general ansatz for the RKMK method is to write the integration step, with ϵ the integration step, as:

$$V_{t+\epsilon} = \exp[\epsilon\Omega(V_t)]V_t \quad (4.20)$$

where $\Omega(V_t)$ is a linear combination of $Z(V_t + \epsilon c_i)$, with c_i the RK coefficients, and of their commutators. Following the suggestion of [19] and considering the analysis of [29] that suggests that, for a fixed step size, an integrator of third order is sufficient. The integration scheme that has been used is the one found in Lüscher's article:

$$\begin{aligned} W_0 &= V_t \\ W_1 &= \exp \left[\frac{1}{4} Z_0 \right] W_0 \\ W_2 &= \exp \left[\frac{8}{9} Z_1 - \frac{17}{36} Z_0 \right] W_1 \\ V_{t+\epsilon} &= \exp \left[\frac{3}{4} Z_2 - \frac{8}{9} Z_1 + \frac{17}{36} Z_0 \right] W_2 \end{aligned} \tag{4.21}$$

where the shorthand notation $Z_i = \epsilon Z(W_i)$ has been introduced. The choice of the coefficients for the Butcher's tableau of the RK method is made in order to satisfy the requirements for a third order RK integrator and to cancel the commutator terms in $\Omega(V_t)$.

What is then left to define are the derivative of the action at a given lattice site and the numerical exponentiation of an $\mathfrak{su}(3)$ element, which returns an $SU(3)$ element.

4.2.1 The Action Derivative

Following the procedure in [30] we define the derivative of the action at a lattice site $U_\mu(x)$ to be:

$$\partial_\mu S[U_\mu(x)] = \frac{i}{2} \left(\Omega_\mu(x) - \frac{1}{3} \mathbb{1} \Im \operatorname{Tr}[\Omega_\mu(x)] \right) \tag{4.22}$$

with

$$\Omega_\mu(x) = U_\mu(x) A_\mu(x) - A_\mu^\dagger(x) U_\mu^\dagger(x) \tag{4.23}$$

where $A_\mu(x)$ are the staples of the link. We can note that the derivative is always traceless hermitean matrix, thus an element of $\mathfrak{su}(3)$ as expected.

4.2.2 Exponential of a $\mathfrak{su}(3)$ Element

Again following [30] we provide a numerical recipe for taking the exponential function of a traceless hermitean 3×3 matrix. The key idea is to use the Cayley-Hamilton theorem, that states that every matrix is a zero of its characteristic polynomial:

$$Q^3 - c_1 Q - c_0 \mathbb{1} = 0, \quad \text{with } c_0 = \det Q = \frac{1}{3}(Q^3), \quad c_1 = \frac{1}{2}(Q^2) \tag{4.24}$$

The exponential of iQ can then be written as:

$$e^{iQ} = f_0 \mathbb{1} + f_1 Q + f_2 Q^2 \tag{4.25}$$

where the functions of the eigenvalues of Q , which in turn can be parameterized, because of the hermitianity of Q in terms of c_0 and c_1 . Labeling the eigenvalues of Q as q_1, q_2, q_3 and using the fact that the matrix is traceless they can be parametrized as:

$$q_1 = 2u \quad q_2 = -u + w \quad q_3 = -u - w \quad (4.26)$$

with:

$$u = \sqrt{\frac{1}{3}c_1} \cos\left(\frac{1}{3}\theta\right) \quad w = \sqrt{c_1} \sin\left(\frac{1}{3}\theta\right) \quad \theta = \arccos\left[\frac{c_0}{2} \left(\frac{3}{c_1}\right)^{3/2}\right] \quad (4.27)$$

As shown in [30] the coefficients f_i can be written as:

$$f_i = \frac{h_i}{9u^2 - w^2} \quad (4.28)$$

with:

$$\begin{aligned} h_0 &= (u^2 - w^2)e^{2iu} + e^{-iu} \left[8u^2 \cos(w) + 2iu(3u^2 + w^2) \frac{\sin(w)}{w} \right] \\ h_1 &= 2ue^{2iu} - e^{-iu} \left[2u \cos(w) - i(3u^2 - w^2) \right] \\ h_2 &= e^{2iu} - e^{-iu} \left[\cos(w) + 3iu \frac{\sin(w)}{w} \right] \end{aligned} \quad (4.29)$$

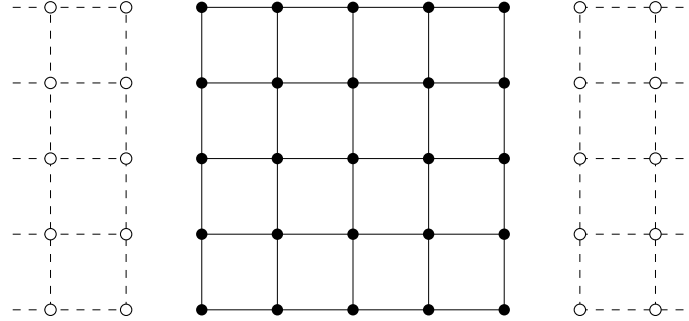
This fairly complicated algorithm is the core of the gradient flow implementation, because fundamentally the integration of the flow equation is a series of matrix exponentials over every action derivative of the lattice.

4.2.3 Parallelization Scheme

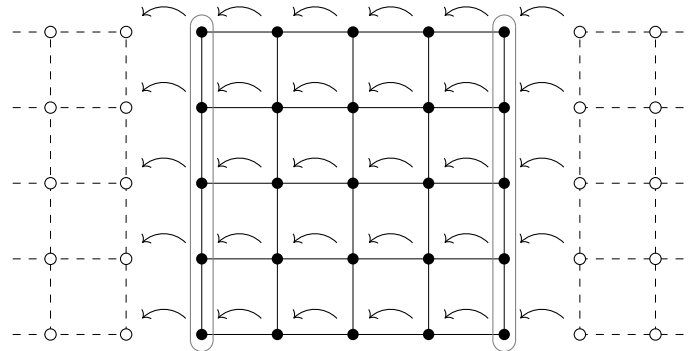
Also this problem is very expensive in computational terms, so it is worth designing a parallelization scheme for it. The idea is still to split the lattice into sub-blocks as in section 4.1.4 and have each processor handle one of them. By looking at eq. (4.21) we see that all operations can be defined on a lattice-wise scale and that they all depend on one previous state of the field, not on an intermediate one as was the case for the generation of gauge fields. This allows us to define a "shift" operation, that effectively creates an additional lattice that is the translation of the original along an axis. The huge advantage is that in order to perform this operation only one communication instance is needed (following the previous scheme in section 4.1.4), but the message is now a whole shared cube between two processors.

An intuitive 2D representation of the shift operation is drawn in fig. 4.3

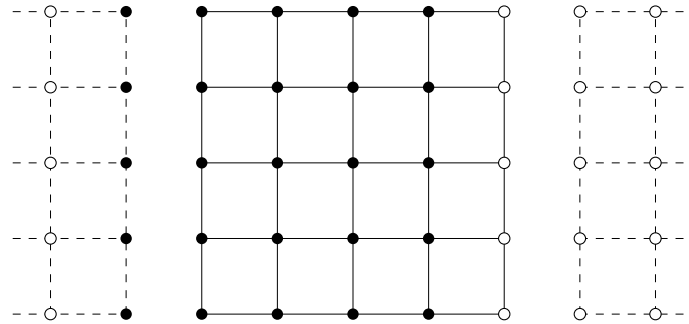
The data to be shifted is on the order of hundreds of kilobytes, which takes some time to be sent by MPI. An optimization that has been implemented is then to rewrite the algorithm in order to use non-blocking communications, first sending the data non-blockingly, then shifting the inner points of the sub-lattice (which do not require links from the neighbors), receiving the data from the neighbor and placing it in the buffer space. **ADD ALGO?**



(a) Normally, one processor only has a local lattice and no data from the neighboring sub-lattices. An empty copy of the sub-lattice is made, to store the shifted lattice.



(b) The shifted lattice is filled with the neighboring links, some of which are received by the “forward” neighbor (so some are sent as well to the “backward” neighbor)



(c) The shifted lattice is now a local object mapped with the same indeces as the original one. A site-by-site multiplication is now possible between the original and the shifted lattices.

Figure 4.3: Parallelization scheme based on lattice shifts. When, for example in the staples computation, a link needs to be multiplied by a neighboring one, a new lattice is created. It is filled with the shifted link, which is fetched either from the local sub-lattice if it is in the central region, or from the neighbors if it is on the edge. This schematic drawing shows how a shift along the “right” direction is performed. A new lattice containing the data of the target link is created by filling it with the target links. The circled regions in fig. 4.3b, the edges, are shared using MPI by first creating a “buffer” of the shape of the edge (it is a cube in the real simulation) and it is sent in a single message to the neighbor which unpacks it in the right location. The new lattice is the multiplied with the original one on a site by site basis, which now is only a local operation.

This has to be implemented for the action derivative lattice and the gauge field itself. The massive reduction in communication overhead, compared to the single link exchange in section 4.1.4, improves the scaling of the algorithm greatly, making this part of the problem much more efficient.

4.3 Structure and Tools

The full code can be found on the web under the link <https://github.com/GioPede>, where both the code for the generation and the flow of gauge fields are hosted. The technical documentation is found at <https://giopede.github.io/LatticeYangMills/html/index.html> and <https://giopede.github.io/LatticeFlow/html/index.html>. As already mentioned the language of choice was C++, mainly because of the high-performance and abstraction level it provides. An object-oriented structure has been used, as can be seen in

FIG: scheme class .

Notable tools that have been used that deserve a mention are MPI, nlhoman/json [31] (used for easy input parameters handling via json files), CMake (for building the project) and Valgrind for function and memory profiling.

Chapter 5

Tests and Runs Description

For

5.1 Generated Ensembles

In order to study the scale parameter, it has been necessary to choose a set of decreasing lattice spacings to then be able to take the continuum limit. The lattice spacing is linked to the coupling g_0 and β by the relation found in eq. (3.4).

We chose 4 values of β that span lattice spacings from approximately 0.1 fm to 0.05 fm in approximately equal steps.

For the calculation to be consistent however, the total volume of the lattice should be kept constant, so the choice of the lattice spacings also determined the number of lattice sites per dimension, having $L = aN \approx const$. The time dimension has been taken to be twice as big as the space dimension. The number of lattice points per dimension, for parallelization's sake, were chosen in order to have many divisors, to allow for different and small sub-blocks.

Table section 5.1 summarizes the physical properties of the ensembles that were generated. For

β	a	$N^3 \times T$	aL [fm]
6.00	0.09314	$24^3 \times 48$	2.23536
6.10	0.07905	$28^3 \times 56$	2.21367
6.20	0.06793	$32^3 \times 64$	2.17405
6.45	0.04781	$48^3 \times 96$	2.29488

Table 5.1: Physical properties of the ensembles used for this work.

each value of β a statistical ensemble was needed. Ideally, one would take as many configurations as possible for each value and in principle one would have the same number of configurations for each of them. However it is clear from the discussion in chapter 4 that the number of lattice sites affects computation times and the capability of storing the configurations dramatically.

Moreover, as will be shown in section 5.2.2 the autocorrelation time of the observables has a non-trivial, power-law or exponential, behavior with the lattice spacing, making the generation of the larger β ensembles even more time consuming.

The following table summarizes the final values for the parameters of the Metropolis algorithm for the different ensembles. These values have been chosen after many tests, checks of the

β	N_{conf}	N_{corr}	MC Steps	N_{hit}	$\epsilon_{SU(3)}$
6.00	1000	600	600000	30	0.25
6.10	500	600	300000	30	0.25
6.20	500	800	400000	30	0.25
6.45	250	1600	400000	30	0.25

Table 5.2: Parameters used for the generation of the ensembles on which the results of this work are based on.

autocorrelation time and mainly in an empirical way. There are some parameters that are free in principle and no real reference study on their impact on the resulting ensemble. In the next section the trial and error approach that led to this decision will be briefly discussed.

5.2 Test Runs

Running some test calculations with a completely new code base is obviously necessary. First some benchmarks to check the expectation values of the observables, both on raw configurations as on flowed configurations. These benchmarks were made using 2 configurations generated with the CHROMA [32] code base from the USQCD collaboration for zero flow-time observables and one configuration flowed using an extension of CHROMA called FlowOps (courtesy of T.Luu and A.Shidler ?correct?), built on QDP++ (the backbone of CHROMA), that applies the Wilson flow to configurations. Both types of test, once all the parameters were made equal, gave results equal to machine precision with the ones generated with the new code base.

Checking the validity of expectation values of observables is a solid indication that the overall back-end of the new code-base has been implemented well, as the results are deterministic. Testing the Metropolis algorithm and assessing the quality of the generated ensembles is much harder, because it involves stochastic computations, hence no numerical check can be easily defined, one can only look at average properties of the ensemble. Unfortunately the generation of gauge field configuration as we saw in section 4.1.5 has 3 parameters that need to be set that do affect the statistical properties of the ensemble, mainly the autocorrelation. As it turns out however, the ϵ parameter, which controls the spread of the $SU(3)$ random elements around the identity matrix, only affects the acceptance ratio, hence the efficiency of the algorithm and not the physical properties (or at least the effects are small).

The tests were all performed on the three largest lattice spacings, as the system for the smallest one is much larger and requires a considerably longer time to compute.

5.2.1 Thermalization

When initializing the Markov Chain, to generate gauge field configurations, one has two options for the initial condition of the link variables of the lattice:

- Hot Start: all links are set to the $SU(3)$ identity element
- Cold Start: all links are set to random $SU(3)$ matrices.

It is easy to see that for the hot start the initial value for the plaquette operator would be 1, when normalized on the lattice volume. For the cold start the initial value is a random number, centered around 0. The Metropolis algorithm is supposed to drive the Markov chain towards the peak of the PDF, eq. (4.9), that is where the action has a minimum.

When computing expectation values using the Monte Carlo integration, it is important to ensure that the sampling of the observables is performed when the Metropolis algorithm reached equilibrium, when it is thermalized. In fig. 5.1 we show that only a small number of MC updates is needed to reach equilibrium (compare the thermalization time of ≈ 600 with the value of N_{corr} from section 4.1.5 and the discussion in section 5.2.2). To ensure thermalization, all results of

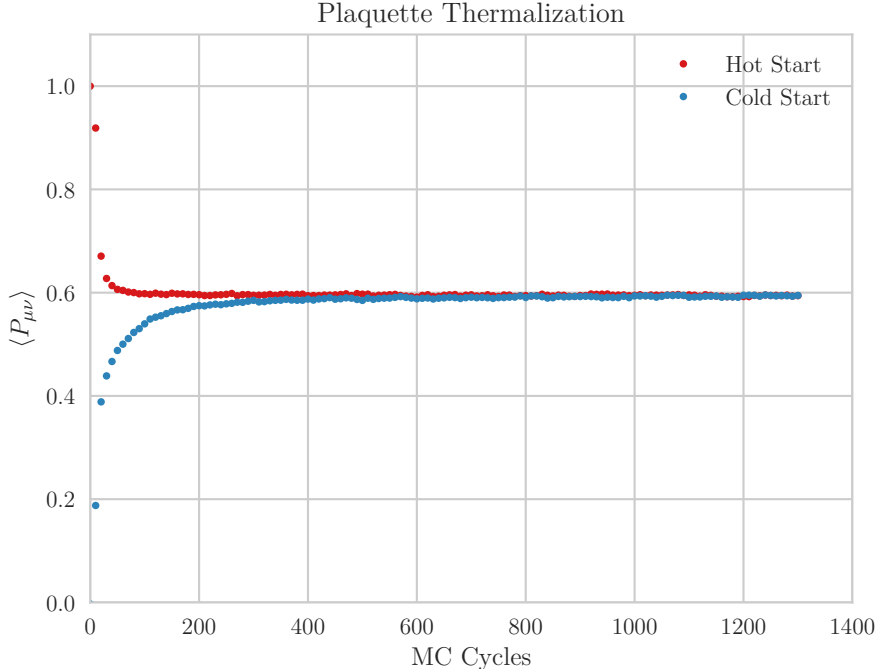


Figure 5.1: Expectation value of the Plaquette as a function of the Monte Carlo updates performed, for hot and cold starts. Equilibrium is reached in both cases after ≈ 600 updates. The data is taken from a simulation with $\beta = 6.10$.

this work are generated discarding the first 10^4 MC cycles, which is much larger than the value

we found, but still a small fraction, so an affordable exaggeration, of the total number of MC cycles of the Markov chain.

5.2.2 Tests on the Autocorrelation of Observables

The most important test has been the assessment of the autocorrelation time for different observables at various lattice spacings varying the parameters of the generation algorithm. As expected, the most problematic quantity is the topological charge, especially at large flow-times. A good measure of how much a data series is autocorrelated is the integrated autocorrelation time τ_{int} , see [Appendix...](#), which is expected to be $1/2$ if the data is uncorrelated. In general, a larger τ_{int} implies an underestimation of uncertainties, so the variance of a quantity is corrected as $\tilde{\sigma}^2 = 2\tau_{int}\sigma^2$.

The first test, in fig. 5.2 shows the integrated autocorrelation time for the topological charge at fixed $N_{corr} = 200$ and $N_{hit} = 10$ for different lattice spacings: Next we looked at a single lattice

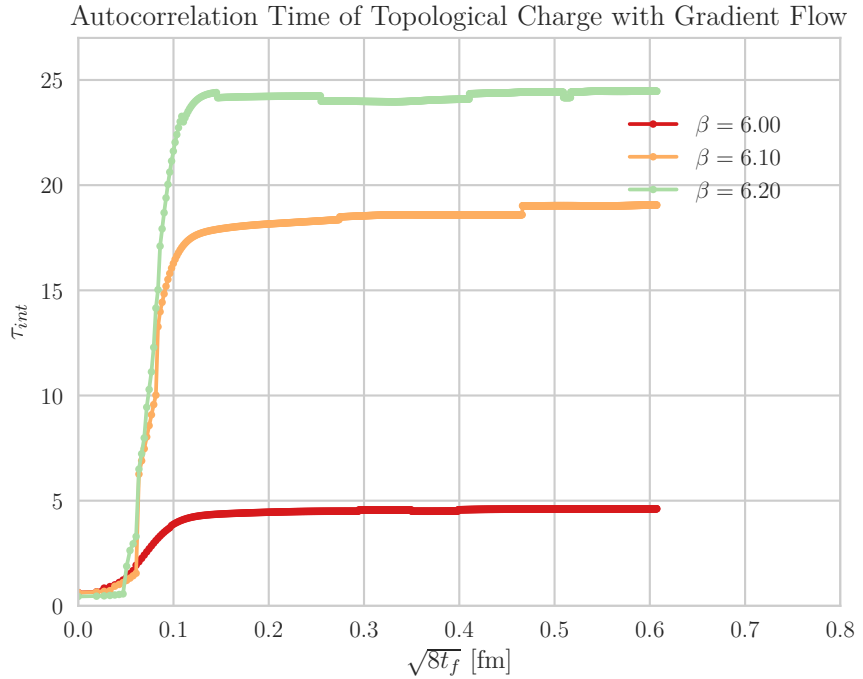


Figure 5.2: Integrated autocorrelation time for $N_{corr} = 200$ and $N_{hit} = 10$ for different inverse coupling values.

spacing and tried to vary the parameters N_{corr} and N_{hits} for the $\beta = 6.10$ case. From the first plot it is clear that the values that were guessed for the parameters N_{corr} and N_{hit} , which could be acceptable for the lowest beta value, are not at all fine for the other lattice spacings. On a general note we observe how the flow quickly removes the low range noise from the observable through the smearing, making it clear that the topological charge is highly correlated in Monte

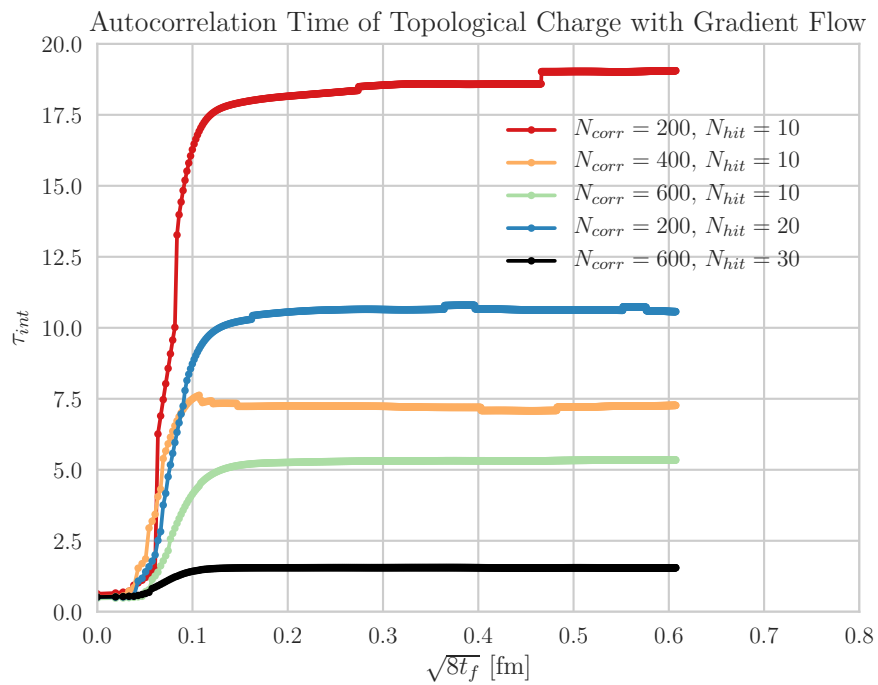


Figure 5.3: Integrated autocorrelation time for $\beta = 6.10$ as the parameters for the gauge field generation N_{corr} and N_{hit} are modified. The black data series represents the chosen set of parameters.

Carlo time even though it might seem uncorrelated if one only looks at $t_f = 0$.

On the other hand, fig. 5.3 suggests a possible cure for the autocorrelation issue. It is almost tautological that increasing the value of N_{corr} decreases the autocorrelation, as the parameter represents how many MC updates are performed between two measurements of the observable. The dependence of τ_{int} from N_{hits} is also clear. From the data we observed that increasing both parameters improved the autocorrelation, so the choice was to set both to a larger value from our initial guess and this proved to be the right choice. The black data series in fig. 5.3 is the data that we used for our analysis, one can notice that it is still autocorrelated, but that can be handled with a reasonable correction to the variance on the data.

It is important to stress again that the autocorrelation is a huge problem mainly for the topological charge. The energy density operator is much less affected and for all the ensembles we generated the integrated autocorrelation time is never a value much greater than 1/2 (see fig. 6.5).

5.2.3 Strong and Weak Scaling

First we can look at the scaling properties of the two sections of the code. We will distinguish the analysis in the two usual quantities used in High Performance Computing for parallel programs: strong and weak scaling.

Strong scaling is the performance of a program measured in execution time as a function of the number of processors used. One would obviously expect the relation to be ideally inverse, with execution time dropping as $1/N_{procs}$, however given the overhead caused by parallelization this is seldomly the case.

Weak scaling is the measure of the performance of a program as the size of the system increases but by keeping the total workload assigned to each processor constant. This measure is important to assess the quality of the parallelization scheme as it gives insights on how much time is spent in communication as more inter-processor messages are being sent. **FIG: PLOT SCALING COMMENTI...**

5.3 Production Runs and Timing

All production runs were carried out on the High Performance Computing Center at Michigan State University (MSU), with the support of the Institute for Cyber-Enabled Research (iCER). Development was performed on local machines and on the small cluster SMAUG located at the Department of Physics of the University of Oslo (UiO) and some larger benchmarks were run on the Abel Computer Cluster also at UiO.

The final ensembles were generated using the parameters in table section 5.3, shows the computing resources used for the generation of all four ensembles.

β	N_{procs}	Wall Time	CPU Time
6.00	1000	600	600000
6.10	500	600	300000
6.20	500	800	400000
6.45	250	1600	400000

Table 5.3: Execution times for generating ensembles from section 5.1 with parameters found in section 5.1. All the runs were performed on the iCER cluster at MSU. N_{procs} is the number of processors used for each ensemble; the Wall Time is the “wall clock” time (the time spent in the parallel execution); CPU time is the product of Wall Time and N_{procs} and represents the actual computation time spent.

Part III

Data Analysis and Results

Chapter 6

Raw Observables

In this chapter the results for simple observables obtained from the ensembles in section 5.1 are presented. Throughout the chapter, all error estimates associated to expectation values of observables have been computed using the bootstrap method, see (REFLINK NEEDED) appendix, which is a popular resampling method used when the sample size of a statistical population is small, as is our case. The autocorrelation, introduced by the Markov chain, is handled using the procedure found in (REFLINK NEEDED) as a correction to the error estimate.

6.1 Plaquette and Energy Density

The plaquette, eq. (2.15), and the energy density, eq. (2.36), are tightly related as they both are estimates of the action. We have already seen in section 5.2.1 that the plaquette can be used to check whether the metropolis algorithm has thermalized in the early stages of the chain. Another test is to check the dependence of the plaquette on the β value of the gluonic action. Since the system is expected, after thermalization, to be in a stationary point of the action, one would then expect the Markov chain to be at equilibrium, so the sampling of the plaquette and of the energy density should be rather constant in Monte Carlo time. Figure 6.2 shows that this is indeed the case. When applying the gradient flow the configuration is evolved towards the minimum of the action, that implies that the values for sufficiently large flow-times are both lattice spacing and flow-time independent. The results do indeed suggest that this is the case:

Moving to the integrated autocorrelation time for the different ensembles, which we report only for the energy as for the plaquette is almost identical. For all ensembles the value of τ_{int} never exceeds 1, meaning that the autocorrelation of the data is not large. Nevertheless, all results of this work (including fig. 6.3 and fig. 6.4) have variances corrected by $\tilde{\sigma}^2 = 2\tau_{int}\sigma^2$.

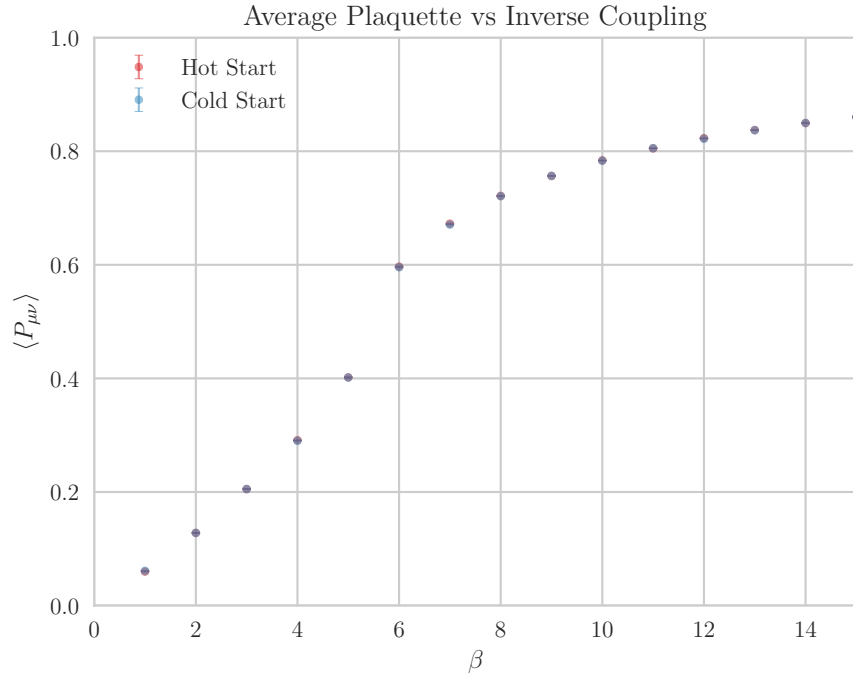


Figure 6.1: Average Plaquette value as a function of the inverse coupling β .

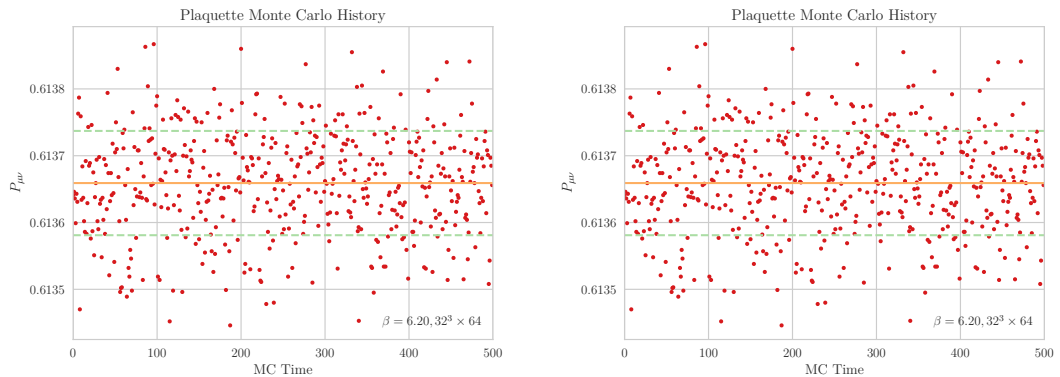


Figure 6.2: Plaquette and Energy Density as a function of Monte Carlo Time. The blue line is the average and the green dashed lines are the 1σ interval around it.

6.2 Topological Charge

A more interesting quantity to measure is the topological charge. In the continuum it is an integer, with a somewhat gaussian spread around zero, though there are studies that prove that indeed it is not a normal distribution ([CITATION NEEDED](#)). The gradient flow removes the divergencies given by the discretization effect, in fig. 6.6 the flow-time evolution of three of

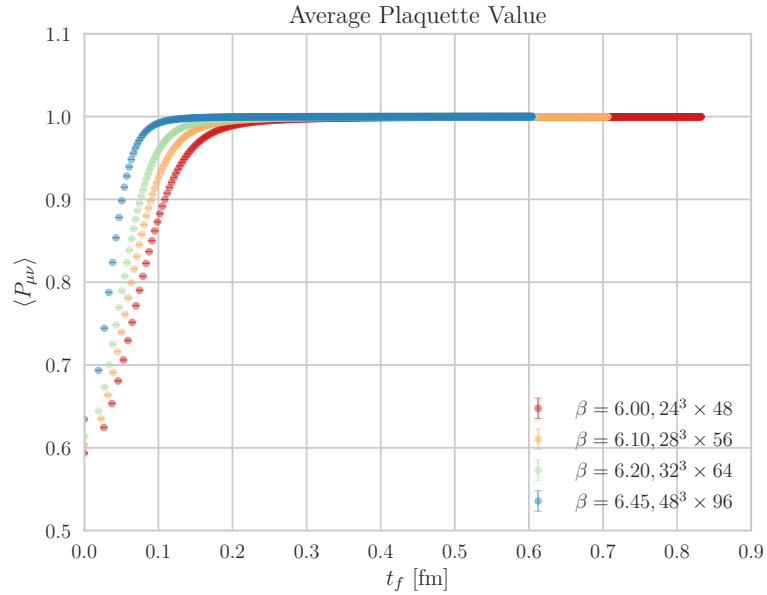


Figure 6.3: Average plaquette value as a function of flow-time t_f .

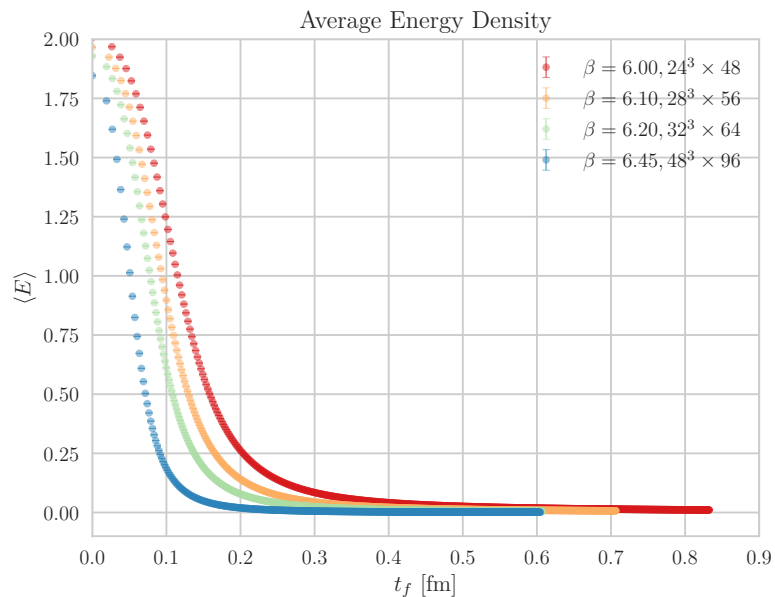


Figure 6.4: Average energy density as a function of flow-time t_f .

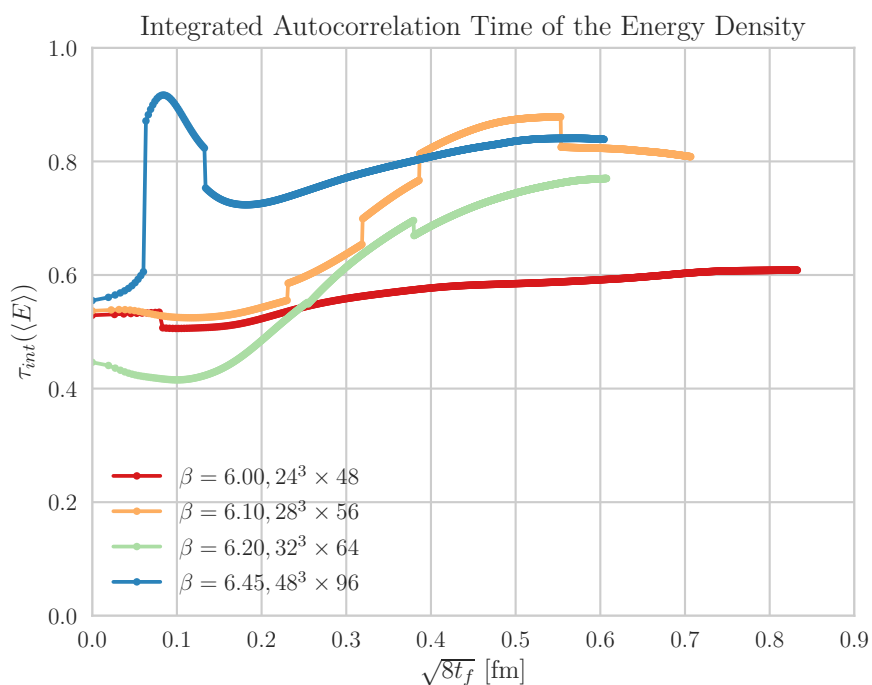


Figure 6.5: Integrated autocorrelation time of the Energy Density as a function of flow-time. The discontinuity of the data is given by the approximation given by the truncation procedure described in APPENDIX

single configurations is plotted, as an example. We can notice that the value of the topological charge has a plateau at a total smearing of roughly 0.2 fm for all cases. For some configurations

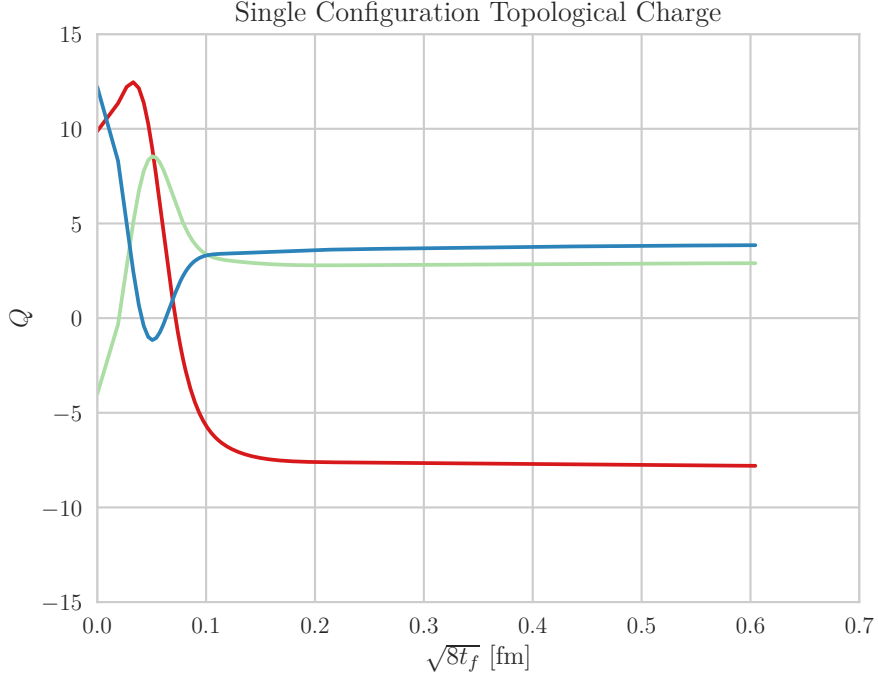


Figure 6.6: Evolution of the topological charge for three single gauge field configurations, taken at random from the $\beta = 6.10$ ensemble.

however, the plateau is not clear and defined. The explanation could be the too simple definition that has been used for the gauge field strength tensor. Perhaps an improved definition of the tensor, given for example with a linear combination of 1×1 , 2×1 , 1×2 and 2×2 (or even higher) Wilson Loops could be beneficial.

When taking the average value of the topological charge on all ensembles, we expect the average to be always zero, and from fig. 6.7 one can check that our data for the expectation value of Q is indeed within error-bars always compatible with zero.

We should note that the increasing error-bars, for $\beta = 6.2$ and $\beta = 6.45$ in particular, are given by the decreasing ensemble size and the increasing autocorrelation time. The integrated autocorrelation time is plotted in fig. 6.8, and comparing it with the equivalent plot for the energy density (fig. 6.5) the difference is clear. The topological charge has a much larger autocorrelation time on the lattice, which grows rapidly with the inverse lattice spacing. It should be noted that the value of N_{corr} is much larger for the $\beta = 6.45$ case than all the others, but still the τ_{int} larger by far.

One last interesting consideration on the topological charge is the distribution of the large flow-time value, that is the value it plateaus at. The bins are taken to be centered on integer and

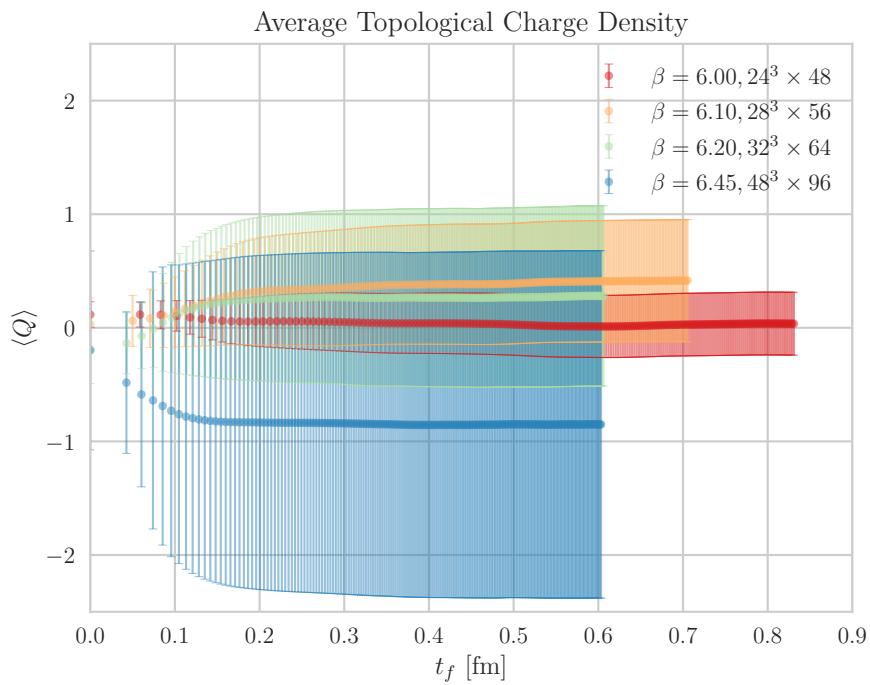


Figure 6.7: Average topological charge value as a function of flow-time t_f . Errorbars are computed using bootstrap and corrected with the integrated autocorrelation time.

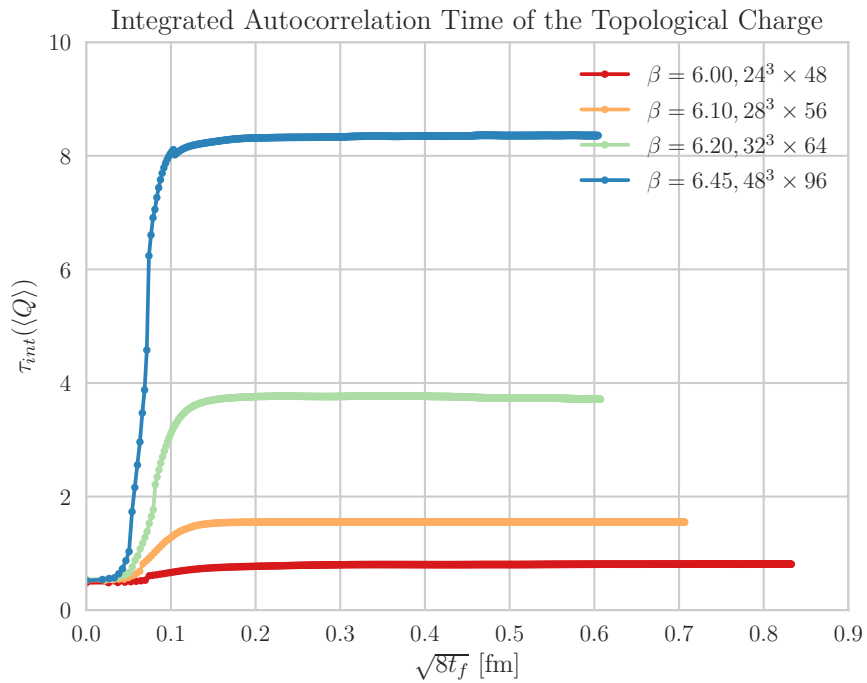


Figure 6.8: Integrated autocorrelation time of the topological charge as a function of flow-time. The ensembles are the ones reported in section 4.1.5, so they have not equal number of cycles between each data point in MC time.

half-integer values in order to capture differences of the distribution of the topological charge. On the lattice it can have also non integer values, but from fig. 6.9 it is possible to see that most of the values, especially at large flow-time (right histogram), are closer to the integer rather than half-integers.

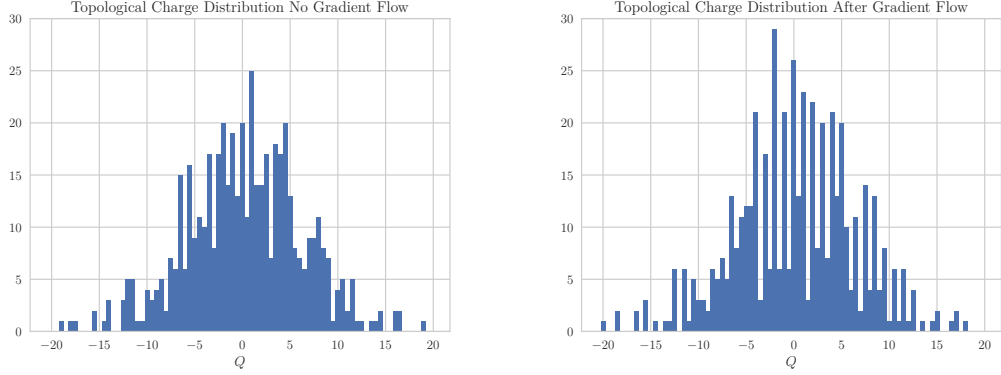


Figure 6.9: Histograms of the topological charge values at $t_f = 0$ (left) and $t_f = 0.6$ (right) for the $\beta = 6.20$ ensemble. The bins are centered on integers and half-integer values.

6.3 Topological Susceptibility

Another quantity that is interesting to measure is the topological susceptibility. Being the average of the squared topological charge it is related to the width of the distributions in fig. 6.9. The evolution with the gradient flow of the susceptibility is not trivial. Its value at non-zero flow-time does not need renormalization, as for all previously mentioned gluonic observables, but at low flow-times the high-frequency fluctuations in the topological charge make it diverge. In order to find the value that effectively reproduces the physical value in the continuum theory one must take the continuum limit.

Here we can see the value of $\chi^{\frac{1}{4}} = \langle Q^2 \rangle^{\frac{1}{4}}$ which in physical units is an energy hence reported in MeV. We notice the fluctuations for low flow-times are removed by the gradient flow. It is then possible to take the continuum limit in a region between 0.4 fm and 0.6 fm. The behavior at zero flow-time is not what we were expecting, comparing to (CITATION NEEDED) we don't observe a clear divergency at $\sqrt{8t_f} = 0$. The behavior seems to be more divergent (a true divergency is impossible, it is always a finite quantity on the lattice) for larger values of β . This could be due to the usage of the clover definition of the gauge field strength tensor, one of the differences between this work and the reference, that perhaps removes low distance noise from the lattice, which contributes to an oversampling of the low topological charge values. This behavior should be investigated SHOULD I REF MATHIAS'S WORK? .

When taking the continuum limit we recover the following value, taken by considering the value of the susceptibility around $\sqrt{8t_f} = 0.5$:

$$\chi^{\frac{1}{4}} = 186.9(4.9) \text{ MeV} \quad (6.1)$$

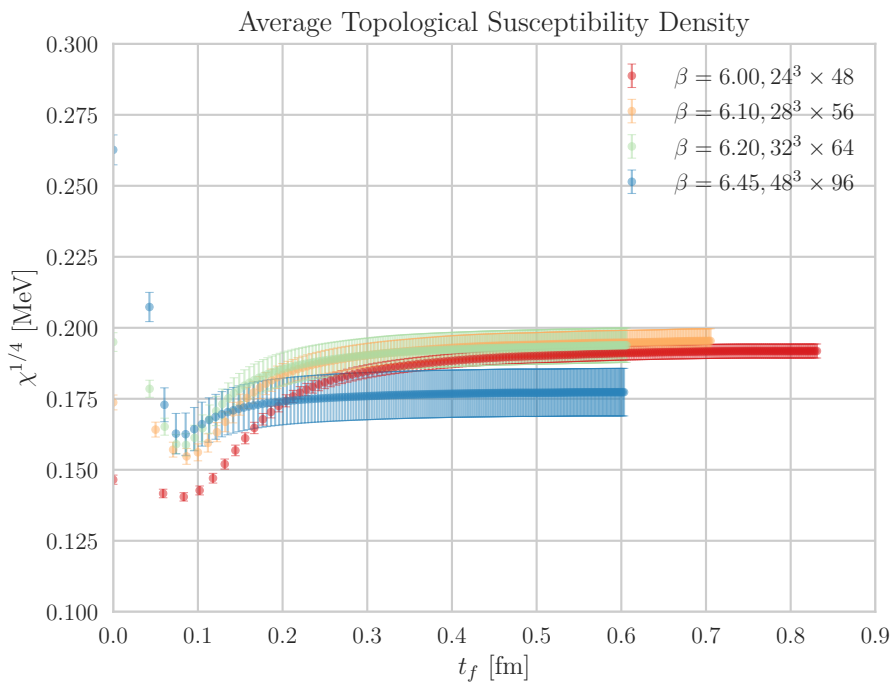


Figure 6.10: Average topological charge value as a function of flow-time t_f . Errorbars are computed using bootstrap and corrected with the integrated autocorrelation time.

This is compatible with the value in (CITATION NEEDED) of As an additional result we

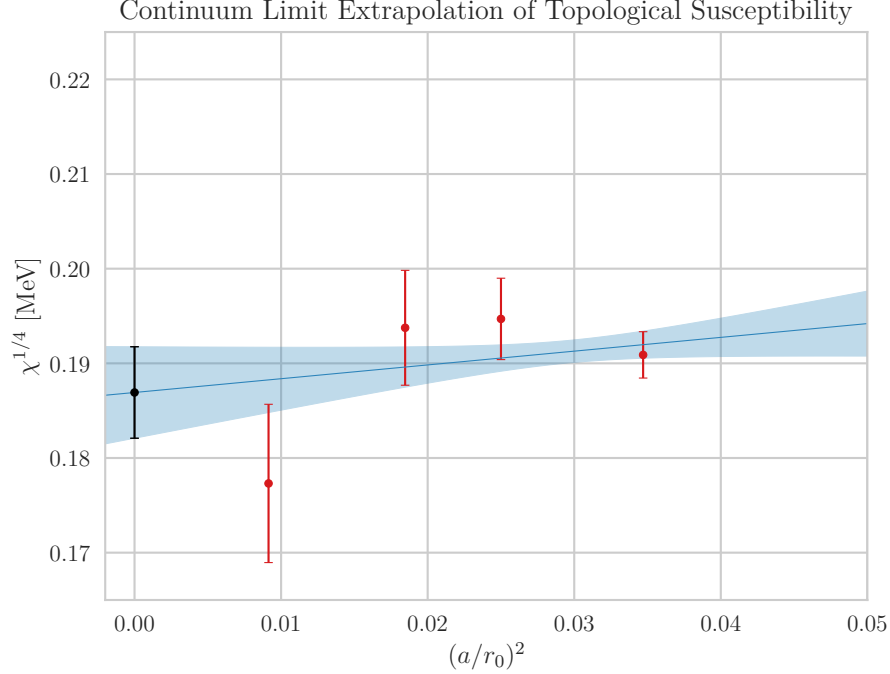


Figure 6.11: Continuum limit extrapolation of $\chi^{\frac{1}{4}}$. The black point is the extrapolated point.

can use this extrapolation to compute the mass of the η' meson taken from the Witten-Veneziano formula:

$$\chi = \frac{F_\pi^2 m_{\eta'}^2}{2N_{flavors}} \quad (6.2)$$

Using as inputs $F_\pi = 92$ MeV, the pion decay constant and having $N_{flavors} = 3$ naturally, the η' mass is:

$$m_{\eta'}^{(lattice)} = \sqrt{\frac{\chi^{\frac{1}{4}} 2N_{flavors}}{F_\pi^2}} = 921(16) \text{ MeV} \quad (6.3)$$

which we compare with an experimental value $m_{\eta'}^{(exp)} = 957.78(6)$ MeV, so we are off by more than 2σ , but probably the result is largely influenced by the data point obtained from $\beta = 6.45$, which has less statistics (only 250 configurations) and larger uncertainty.

Chapter 7

Running Coupling and Scale Fixing

In section 3.3 the perturbative behavior of the expectation value of $t_f^2 \langle E \rangle$ was introduced. In this chapter the same quantity is studied from the data generated from our ensembles of lattice gauge field configurations, for which the code-base was developed. The matching between the perturbative and lattice results will also be discussed.

7.1 Discretization Effects on $t_f^2 \langle E \rangle$

Plotting the data for the average value of the energy as a function of the dimensionless quantity t_f/r_0^2 ($r_0 = 0.5$ is the Sommer parameter, described in section 3.3.1 and has unit of length) many interesting properties can be observed. Firstly, the data suggests that for $t_f > 0.05r_0$ is lattice spacing independent, and so coupling independent since they are related. This allows, as it was suggested by [19] that this quantity can be used to set the reference scale of the lattice, similarly to r_0 . By selecting a value for $t_f^2 \langle E \rangle$ one can create a reference scale. It was proposed to use the value of 0.3, which from the plot we can see that is in the region of best matching between the different data series.

In an operative way one finds the value of the flow-time t_0 for which:

$$t_0 \langle E \rangle = 0.3 \quad (7.1)$$

This value, in this work, is found by selecting the 20 points, for each data series corresponding to a different β value, and fitting a straight line through them. By inverse regression the value of t_0 and its uncertainty are found.

We can then check the validity of the assumptions, plot the analog of fig. 3.3 in which the ratio of $\sqrt{8t_0}/r_0$, that is the rate of the tentative scale based on the gradient flow and the Sommer parameter. If this ratio is independent from the lattice spacing then $\sqrt{8t_0}$ can be used as a reference scale r_0 . With this procedure we fix a value of $\sqrt{8t_0}/r_0$ to be:

$$\sqrt{8t_0}/r_0 = 0.9499(8) \quad (7.2)$$

which is compatible with the values found in (CITATION NEEDED).

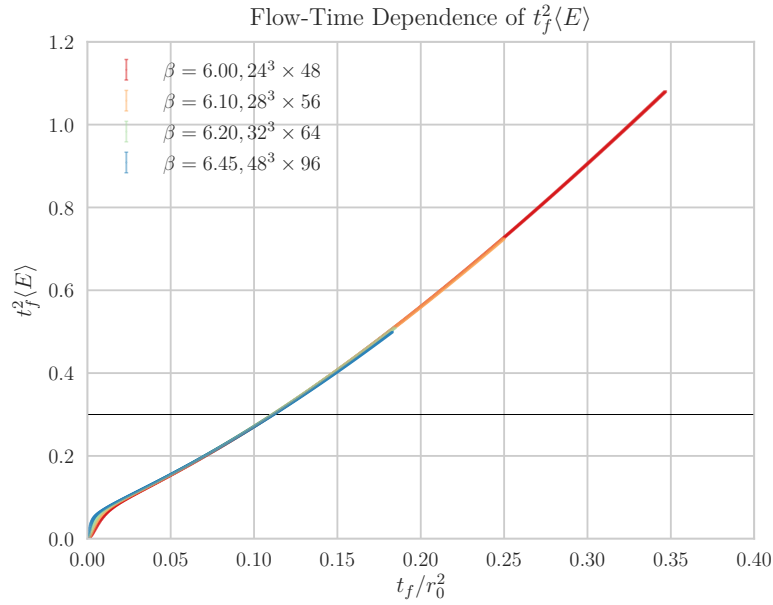


Figure 7.1: $t_f^2 \langle E \rangle$ computed on the four ensembles that were generated (section 4.1.5) as a function of the flow-time in units of r_0^2 . The solid line is for $t_f^2 \langle E \rangle = 0.3$

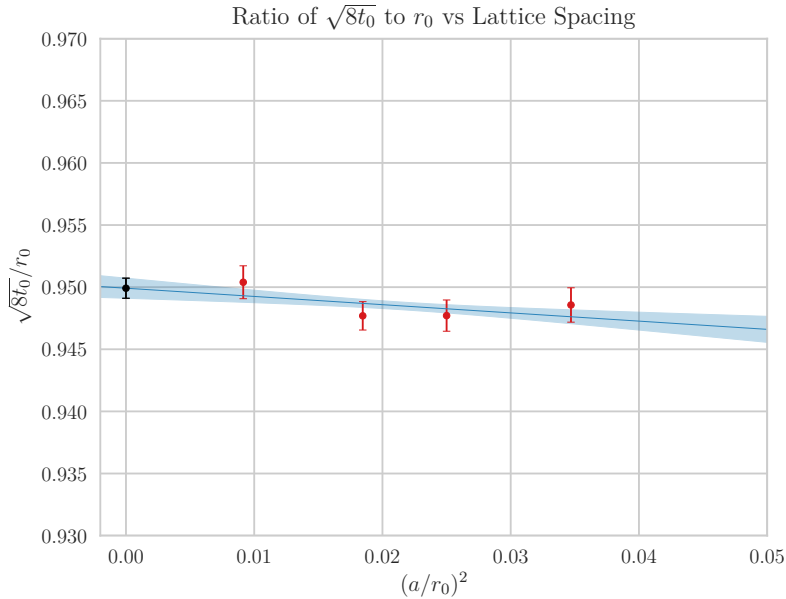


Figure 7.2: Continuum limit extrapolation of the ratio $\sqrt{8t_0}/r_0$. The solid line is the linear fit of the data points, each representing a different β value. The errorband is the 1σ confidence interval and the black point is the extrapolated continuum point.

7.2 Matching Perturbative and Lattice Results

When focusing on the low flow-time section of the $t_f^2 \langle E \rangle$ plot, one can study the matching between the perturbative expansion of the observable, performed in [19], and the lattice results that we generated.

The greatest challenge however is that the flow-time interval in which this matching happens is unknown. Certainly for large t_f perturbation theory fails to describe the system: any perturbative expansion in $\alpha_s(q)$ becomes meaningless, as $q = 1/\sqrt{8t_f}$ becomes small the coupling grows and approaches one. For small flow-times the lattice results become unreliable, in the region where the smearing radius is much smaller than the lattice spacing; this is clear by looking at a zoomed version of fig. 7.1. Both of these two bounds, no matter how intuitive they appear, are also not clearly defined and so no unique procedure can be found to constrain the matching region.

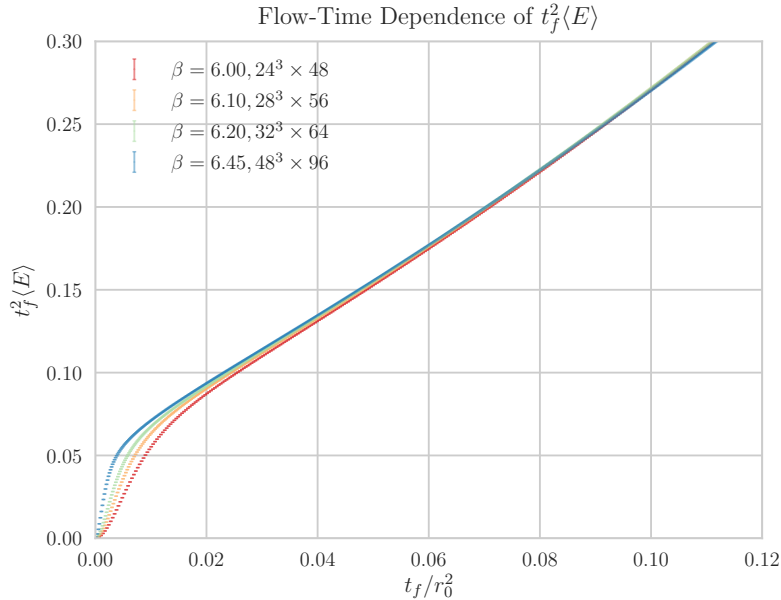


Figure 7.3: Detail of fig. 7.1 for small flow-times.

7.2.1 Strategy for the Estimation of the Scale Energy Λ

The problem we are interested to solve is to extract the value of the scale energy of Yang-Mills theory from the lattice data. The only link between the two is eq. (7.3). If the equation is rewritten as:

$$t_f^2 \langle E \rangle = \frac{3}{4\pi} \alpha_s(q) [1 + k_1 \alpha_s(q) + \mathcal{O}(\alpha_s^2)], \quad k_1 = 1.0978 + 0.0075 \times N_f \quad (7.3)$$

one can compute the left hand side on the lattice and fit it to the analytical expression on the

right hand side from perturbation theory.

As mentioned earlier the problem is to determine matching region, which now affects the fit range. This must be done carefully in order to prevent possible biases and to assess the error on Λ properly.

Part IV

Conclusions

Chapter 8

Summary and Outlook

Part V

Appendices

Appendix A

Statistical Tools

something here...

Bibliography

- [1] UX: Standard Model of the Standard Model, November 2013.
- [2] Schroder Peskin. *An Introduction to Quantum Field Theory*. Cambridge University Press, 1989.
- [3] Shahida Dar. The Neutron EDM in the SM : A Review. *arXiv:hep-ph/0008248*, August 2000. arXiv: hep-ph/0008248.
- [4] A Chaudhuri. A short course on relativistic heavy ion collisions. 07 2012.
- [5] G Dissertori. 9. QUANTUM CHROMODYNAMICS. page 50, 2016.
- [6] David J. Gross and Frank Wilczek. Ultraviolet behavior of non-abelian gauge theories. *Phys. Rev. Lett.*, 30:1343–1346, Jun 1973.
- [7] H. David Politzer. Reliable perturbative results for strong interactions? *Phys. Rev. Lett.*, 30:1346–1349, Jun 1973.
- [8] R Machleidt and F Sammarruca. Chiral EFT based nuclear forces: achievements and challenges. *Physica Scripta*, 91(8):083007, August 2016.
- [9] S.K. Bogner, R.J. Furnstahl, and A. Schwenk. From low-momentum interactions to nuclear structure. *Progress in Particle and Nuclear Physics*, 65(1):94–147, July 2010.
- [10] Kenneth G. Wilson. Confinement of quarks. *Physical Review D*, 10(8):2445–2459, October 1974.
- [11] Christof Gattringer and Christian B. Lang. *Quantum Chromodynamics on the Lattice*, volume 788 of *Lecture Notes in Physics*. Springer Berlin Heidelberg, Berlin, Heidelberg, 2010.
- [12] Rajan Gupta. Introduction to Lattice QCD. *arXiv:hep-lat/9807028*, July 1998. arXiv: hep-lat/9807028.
- [13] E. Witten. Current algebra theorems for the U(1) Goldstone boson. *Nuclear Physics B*, 156(2):269–283, September 1979.
- [14] Adriano Di Giacomo. Topology in lattice QCD, November 1997.

- [15] Constantia Alexandrou, Andreas Athenodorou, Krzysztof Cichy, Arthur Dromard, Elena Garcia-Ramos, Karl Jansen, Urs Wenger, and Falk Zimmermann. Comparison of topological charge definitions in Lattice QCD. *arXiv:1708.00696 [hep-lat]*, August 2017. arXiv: 1708.00696.
- [16] David J. Gross, Robert D. Pisarski, and Laurence G. Yaffe. QCD and instantons at finite temperature. *Reviews of Modern Physics*, 53(1):43–80, January 1981.
- [17] R. Sommer. A New Way to Set the Energy Scale in Lattice Gauge Theories and its Application to the Static Force and $\text{\textbackslash textbackslash alpha_s}$ in SU(2) YangMills Theory. *Nuclear Physics B*, 411(2):839–854, January 1994. arXiv: hep-lat/9310022.
- [18] M. Guagnelli, R. Sommer, and H. Wittig. Precision computation of a low-energy reference scale in quenched lattice QCD. *Nuclear Physics B*, 535(1):389–402, December 1998. arXiv: hep-lat/9806005.
- [19] Martin Lüscher. Properties and uses of the Wilson flow in lattice QCD. *Journal of High Energy Physics*, 2010(8), August 2010.
- [20] Martin Lüscher and Peter Weisz. Perturbative analysis of the gradient flow in non-abelian gauge theories. *Journal of High Energy Physics*, 2011(2), February 2011. arXiv: 1101.0963.
- [21] Martin Lüscher. Chiral symmetry and the YangMills gradient flow. *Journal of High Energy Physics*, 2013(4), April 2013. arXiv: 1302.5246.
- [22] Martin Lüscher. Erratum: Properties and uses of the Wilson flow in lattice QCD. *Journal of High Energy Physics*, 2014(3), March 2014.
- [23] G Dissertori. 9. QUANTUM CHROMODYNAMICS. page 50, 2016.
- [24] T. van Ritbergen, J. A. M. Vermaasen, and S. A. Larin. The four-loop beta-function in Quantum Chromodynamics. *Physics Letters B*, 400(3):379–384, May 1997. arXiv: hep-ph/9701390.
- [25] Nicholas Metropolis, Arianna W. Rosenbluth, Marshall N. Rosenbluth, Augusta H. Teller, and Edward Teller. Equation of State Calculations by Fast Computing Machines. *The Journal of Chemical Physics*, 21(6):1087–1092, June 1953.
- [26] Hans Munthe-Kaas. Runge-Kutta methods on Lie groups. *BIT Numerical Mathematics*, 38(1):92–111, March 1998.
- [27] Hans Munthe-Kaas. Lie-Butcher theory for Runge-Kutta methods. *BIT Numerical Mathematics*, 35(4):572–587, December 1995.
- [28] Elena Celledoni, Hkon Marthinsen, and Brynjulf Owren. An introduction to Lie group integrators basics, new developments and applications. *Journal of Computational Physics*, 257:1040–1061, January 2014.
- [29] Marco C, Cristian Consonni, Georg P. Engel, and Leonardo Giusti. Non-Gaussianities in the topological charge distribution of the SU(3) Yang-Mills theory. *Physical Review D*, 92(7), October 2015.

- [30] Colin Morningstar and Mike Peardon. Analytic smearing of SU (3) link variables in lattice QCD. *Physical Review D*, 69(5), March 2004.
- [31] json/index.md at develop nlohmann/json.
- [32] Robert G. Edwards and Balint Joo. The Chroma Software System for Lattice QCD. *Nuclear Physics B - Proceedings Supplements*, 140:832–834, March 2005. arXiv: hep-lat/0409003.